

Magnetic Reconnection Studies on SSX

Thomas W. Kornack

kornack@earthling.net

Swarthmore College Department of Physics and Astronomy

500 College Avenue, Swarthmore, PA 19081

June 10, 1998

Abstract

Magnetic reconnection is the fundamental process by which magnetic fields in conductive fluids topologically rearrange themselves while moving to a lower energy state. Merging two parcels of magnetofluid with oppositely oriented magnetic fields causes the fields to be annihilated. Conservation of energy demands that magnetic energy be converted into the kinetic energy of the fluid, which is accelerated out of the reconnecting layer. The Swarthmore Spheromak Experiment (SSX) studies magnetic reconnection by merging two rings of plasma magnetofluid called spheromaks. The magnetic reconnection is observed using magnetic probes and the accelerated particles are measured using particle detectors. Magnetic reconnection events have been observed and show strong correlation with high energy particle flow out of the reconnecting layer of plasma. 1D and 2D maps of the time resolved magnetic field in the reconnection region are presented, showing the evolution of both X-points and O-points. These observations are used to compare various analytical and numerical models of reconnection. The Sweet-Parker (Sweet, 1958; Parker, 1957) resistive MHD model of reconnection is presented as a simple and well understood theory. Experimental observations of the size of the reconnection layer, however, do not agree with the resistive MHD prediction. A two-fluid collisionless theory by Biskamp et al. (1997) provides a good prediction of the scaling and a more detailed picture of the structure of the reconnection layer. Simulations by Matthaeus et al. (1984) show that turbulence can create O-points in the reconnection layer. Whereas these theories provide good macroscopic descriptions of reconnection, the actual physical mechanism for reconnection at the microscopic scale remains unknown. This thesis also includes supporting material on a fast gas valve design, triple probe analysis, and spheromak formation studies in the appendices.



Contents

| | | |
|--------------------|--|-----------|
| 1 | Introduction | 1 |
| 2 | Reconnection in Astrophysical Plasmas | 3 |
| 3 | Basic Plasma Physics | 6 |
| 3.1 | The Magnetic Induction Equation | 7 |
| 3.2 | Frozen-In Flux Constraint | 9 |
| 4 | Reconnection Theory | 11 |
| 4.1 | Incompressible Fluid Model (Sweet-Parker) | 11 |
| 4.2 | Collisionless Reconnection (Biskamp and Drake) | 15 |
| 4.3 | Turbulent Reconnection Layers (Matthaeus) | 18 |
| 5 | Spheromak Plasmas | 20 |
| 6 | Experimental Setup | 23 |
| 6.1 | Magnetic Probes | 27 |
| 6.2 | Retarding Grid Energy Analyzer | 29 |
| 7 | Experimental Results | 31 |
| 7.1 | Linear Probe Results | 31 |
| 7.2 | RGEA Results | 35 |
| 7.3 | 2D Data | 37 |
| 8 | Concluding Remarks | 40 |
| <i>Appendicies</i> | | |
| A | Derivation of the Generalized Ohm's Law | 41 |
| B | Triple Probe Measurements | 43 |
| C | The Spheromak Formation Threshold | 47 |
| D | Fast Pulse Gas Valve Design | 50 |
| E | Acknowledgements | 53 |
| | References | 54 |

List of Figures

| | | |
|----|---|----|
| 1 | Schematic of magnetic reconnection | 2 |
| 2 | Coronal loop picture | 4 |
| 3 | Coronal loop magnetic reconnection | 4 |
| 4 | Magnetic induction equation illustration | 9 |
| 5 | Frozen-in flux calculation illustration | 10 |
| 6 | Sweet-Parker model illustration | 12 |
| 7 | Thin current sheet evolution | 14 |
| 8 | Scaling of terms in Ohm's law | 16 |
| 9 | Collisionless reconnection model illustration | 17 |
| 10 | X-points and O-points | 19 |
| 11 | Spheromak field configuration | 21 |
| 12 | Spheromak formation | 21 |
| 13 | Picture of the lab | 24 |
| 14 | Schematic of experimental apparatus | 24 |
| 15 | Reconnection using spheromaks | 25 |
| 16 | Linear magnetic probe | 26 |
| 17 | Forest magnetic probe | 26 |
| 18 | Picture of the Kornack gas valve | 27 |
| 19 | Magnetic probe design | 28 |
| 20 | Energetic ion detector (RGEA) | 30 |
| 21 | Run #13(97/10/8): Low resolution magnetic data | 32 |
| 22 | Run #13(97/10/8): Particle flux in reconnection plane | 32 |
| 23 | Run #13(98/1/26): High resolution magnetic data | 34 |
| 24 | Run #13(98/1/26): Particle flux out of reconnection plane | 34 |
| 25 | Run #14(98/1/26): Width of layer measurement | 35 |
| 26 | Ion energy spectra | 36 |
| 27 | Run #05(98/4/20): Forest probe data | 38 |
| 28 | Triple probe schematic | 46 |
| 29 | Triple probe response curves | 46 |
| 30 | Triple probe temperature and density data | 46 |
| 31 | Formation threshold model | 49 |
| 32 | Formation threshold data | 49 |
| 33 | Gas valve design | 52 |
| 34 | Fast Ionization Gauge (FIG) data | 52 |

List of Tables

| | | |
|---|---------------------------------|----|
| 1 | SSX Plasma Parameters | 27 |
|---|---------------------------------|----|

1 Introduction

Magnetic reconnection in magnetofluids is the process by which lines of magnetic force break and rejoin in a lower energy state. The excess energy appears as kinetic energy of the plasma at the point of reconnection. Experiments performed at the Swarthmore Spheromak Experiment (SSX) probe the properties of magnetic reconnection in order to better understand this fundamental process in plasma physics.

Figure 1 shows the configuration of magnetic fields in a region where magnetic reconnection is taking place. The reconnecting field lines form an X-point at the center where the topology changes from being connected horizontally to being connected vertically. The double arrows show flow velocity, indicating that parcels of plasma with oppositely oriented magnetic fields are merged together. The oppositely oriented magnetic field vectors annihilate each other. By conservation of energy, the plasma where the field was annihilated is accelerated outwards to a characteristic speed, called the Alfvén speed. Conservation of energy does not, however, specify the detailed structure of the magnetic field in the reconnection region or provide a physical mechanism for the breaking of field lines. Many theories have been proposed to answer these questions.

This thesis explores three major theories of magnetic reconnection. The Sweet-Parker model (Sweet, 1958; Parker, 1957) is an analytical model that is based on resistive magnetohydrodynamics and uses the conservation of energy argument used above. The collisionless reconnection model, proposed by Biskamp et al. (1997), shows that dynamic forces ignored by the Sweet-Parker model are significant and cannot be omitted to fully describe the structure of magnetic reconnection. A third theory by Matthaeus et al. (1984) shows that turbulence in the reconnection layer creates “magnetic bubbles” out of which a small number of very high energy particles can escape perpendicular to the plane of the reconnecting magnetic field. Section 4 contains a detailed description of each of these theories.

The experiments supporting this thesis are designed to test these theories. Magnetic reconnection is generated by merging two spheromaks, which are unlinked toroidal configurations of magnetofluids. Spheromaks have large magnetic fields and low pressure effects, making them a good candidate for magnetic reconnection studies. Because it is unlinked, the spheromaks can be created at the ends of the vacuum chamber and then translated to the region in the center where the experiment takes place. This freedom allows the sources of electromagnetic noise in the spheromak formation regions to be removed from the experiment. Tokamaks, stellarators, and many other plasma confinement schemes are linked by the device and cannot be moved so easily. Magnetic probes are used to produce maps of the magnetic structure as a function of time. An energetic particle detector simultaneously measures the energetic ion flux as a function of time. The energy spectrum is measured for particles emitted perpendicular and parallel to the plane of reconnection. Measurements with these two devices are used to check the predictions of various theories.

Recent laboratory experiments by Yamada et al. (1991) and Ono et al. (1993) also use spheromaks to probe magnetic reconnection. They have shown the importance of the three dimensional structure of the reconnecting magnetic field on the rate of reconnection. They have also observed ion acceleration and plasma heating due to magnetic reconnection. None of the experiments, however, has observed the directionality of the accelerated ions from the reconnection region.

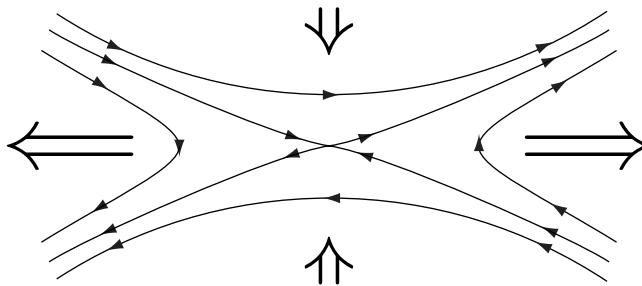


Figure 1: Schematic of magnetic reconnection. Single line arrows are magnetic field and double line arrows indicate magnetofluid flow velocity. The merging of two magnetofluids with oppositely oriented magnetic fields causes the fields to annihilate. The excess energy accelerates the plasma out of the reconnection region in the direction of the long double line arrows. Note the characteristic X-point where the topology changes for two field lines.

Magnetic reconnection studies are relevant to solar and magnetotail physics and to the fusion program. It is widely believed that magnetic reconnection plays an important role in the dynamics of solar flares and may be the primary heating mechanism in the solar corona. Reconnection in the earth's magnetotail causes particles to be accelerated earthward. These topics are discussed in the astrophysical plasmas section (section 2). Tokamak plasmas like those commonly found in the fusion program are subject to repeated reconnection events as the magnetofluid equilibrium evolves. The signature of this reconnection is a sawtooth signal from magnetic field probes and many other measurements. Sudden magnetic reconnection events in fusion reactors can be very dramatic and can cause disruptions of the plasma. Such disruptions prevent steady state fusion reactions and can damage the reactor. The study of magnetic reconnection may help predict the rate of sawtooth signals and may indicate how such disruptions can be minimized.

This thesis is organized into eight sections and five appendices. The introduction is followed by a discussion of the role of magnetic reconnection in astrophysical plasmas. Section 3 presents derivations of essential basic plasma physics equations and parameters. These results are applied to theories of magnetic reconnection in section 4. Section 5 describes spheromak formation and equilibrium, and the details of the experiment are presented in section 6. The results are presented in section 7 followed by a conclusion in section 8.

2 Reconnection in Astrophysical Plasmas

There is growing evidence that reconnection processes control the release of energy into the solar corona. Figure 2 shows a visible light picture of a “coronal loop” emanating from the surface of the sun. Coronal loops have strong currents flowing through them and are confined by their own magnetic fields. Recent satellite observatories such as Yohkoh and SOHO have produced dramatic images of coronal loops in hard and soft x-ray as well as visible light. Using these instruments, Masuda et al. (1994) identified the spectral signature of particle acceleration due to magnetic reconnection at the top of the coronal loops. According to his theory, the coronal loop is distended by buoyancy¹, which causes the top of the loop to distend and reconnect as shown in figure 3. Particles in the reconnection region accelerate towards the surface of the sun and out away from the sun. Those particles that are accelerated back towards the sun are confined within the loop’s magnetic field and follow the field lines down to the footpoints of the loop where the accelerated particles collide with other particles and lose their energy through x-ray emissions.

The emission of energetic particles at the top of the loop may help explain why the corona (upper atmosphere) of the sun is three orders of magnitude hotter than the surface of the sun. Measurements of emission spectra show that the surface of the sun is about 5400 K while the corona is more than 10^6 K. It is not possible to explain this temperature difference by thermodynamics alone. Magnetic reconnection provides a mechanism for energy to be transported into the solar corona in the form of magnetic energy and then converted into kinetic energy. A coronal loop such as the one in figure 2 is the most visible manifestations of this energy transport mechanism.

The so-called Masuda flare has subsequently been studied by others in great detail and their results support this theory. Aschwanden et al. (1996) measured bursts of x-rays with periods on the order of seconds coming from the loop-top and footpoints. Timing delays between different x-ray energies in these bursts reveal several acceleration and escape mechanisms for downward flowing particles accelerated by reconnection (Aschwanden et al., 1996, 1995). Shibata (1995) detected jets of upward flowing plasma above the Masuda flare at close to the Alfvén speed, providing further evidence of reconnection and conversion of magnetic energy to kinetic energy. Doppler shift measurements on the SOHO ultraviolet spectrometer show evidence of bidirectional Alfvénic jets in the reconnection plane (Innes et al., 1997).

These coronal loops occur at a frequency that peaks approximately every 11 years (the solar cycle). One might expect that the temperature of the corona varies accordingly. No such fluctuation has been observed, prompting researchers to search further for the coronal heating mechanism. Recent high resolution observations from SOHO show that there are very small scale magnetic structures on the surface of the sun that are constantly undergoing reconnection and releasing energy into the corona (Press Release: <http://soi.stanford.edu/press/ssu11-97/>). The reconnection processes are hypothesized to release energetic particles into the corona on a smaller scale in the same way as the larger coronal loops. These smaller structures do not appear to vary in activity with the solar cycle

¹A magnetic structure is buoyant because it exchanges lower particle density for a larger magnetic energy density (which doesn’t weigh anything). The external (surface or coronal) pressure is therefore balanced by a lower gas pressure in conjunction with a magnetic pressure. Since it has lower density, it is buoyant.

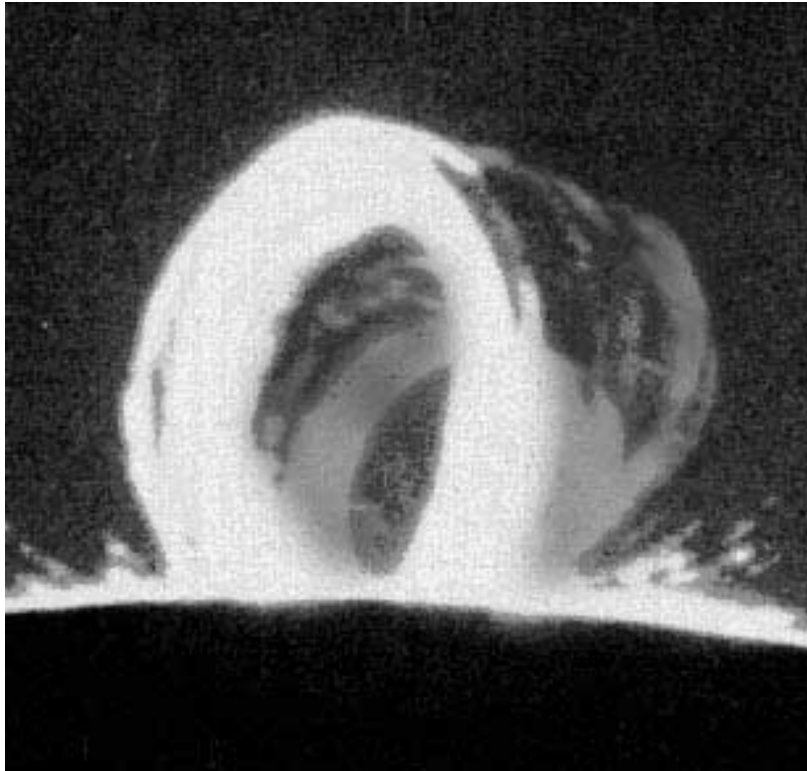


Figure 2: A coronal loop emanating from the surface of the sun. This loop is many earth diameters wide. (source: Skylab?)

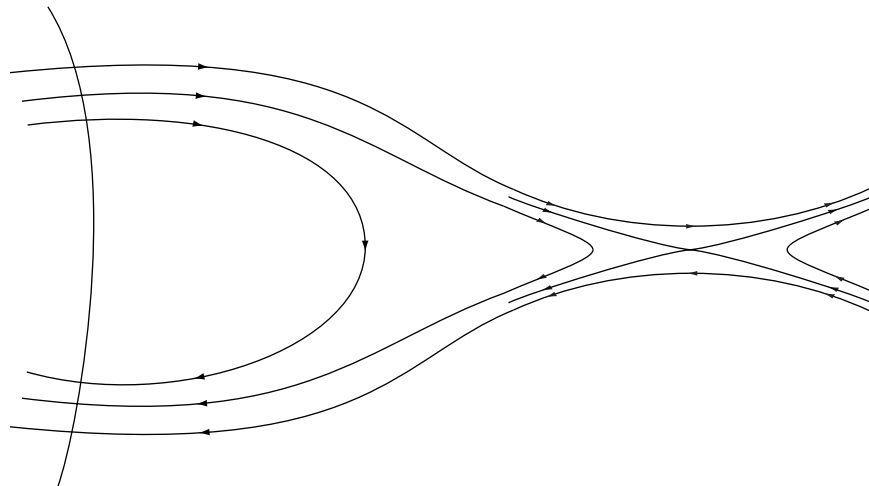


Figure 3: Reconnection due to buoyancy blowing a coronal loop apart. A very similar picture can be drawn for the earth's magnetotail, replacing the source with a dipole field.

and therefore provide a constant energy flux into the corona which maintains the constant temperature of the corona. The total energy flux of the small scale structures is far greater than that of the larger coronal loops.

Magnetic reconnection is also important in the physics of the earth's magnetotail. The solar wind distends the earth's dipole magnetic field so that the field extends behind the earth for many earth diameters. The picture is the same as that shown for the coronal loop in figure 3 with the surface of the sun replaced by the earth's dipole magnetic field. Earthward flowing plasma streams with flow velocities up to 1000 km/s (close to the local Alfvén speed) have been observed after reconnection events in the earth's magnetotail (Birn et al., 1981).

These recent results have fueled interest in the physics of magnetic reconnection. While these solar and magnetotail measurements are becoming very accurate, they are still unable to determine the details of the physical processes. Laboratory plasmas can reproduce the relevant conditions and simulate the reconnection processes that are observed in the Sun and the earth's magnetotail. Laboratory plasmas are controlled and the detailed measurements are much easier to perform. The results from laboratory studies evolve the theory of magnetic reconnection, which can be directly applied to astrophysical phenomena.

3 Basic Plasma Physics

A plasma is a collection of charged particles usually created by ionizing a gas. In SSX, we ionize hydrogen to create a plasma of protons and electrons. Since the electrons are not bound to the protons, the plasma is a good conductor and can carry currents which create magnetic fields. The magnetic and electric fields in a plasma affect the particle motion according to the Lorentz force:

$$\mathbf{F}_{Lorentz} = q(\mathbf{E} + \mathbf{v} \times \mathbf{B}) \quad (1)$$

where \mathbf{v} is the velocity of the particle and q is its charge. The local electric and magnetic field are denoted by \mathbf{E} and \mathbf{B} , respectively. In the absence of a strong electric field, this force causes electrons and ions to orbit around magnetic field lines. The radius of this orbit for a particle of mass m is given by the balance of centripetal acceleration and the Lorentz force:

$$r_{cyclotron} = \frac{mv_{\perp}}{qB} \quad (2)$$

where v_{\perp} is the component of the velocity perpendicular to the magnetic field. If the particles orbit the field lines, then they will not pass out of the magnetic field and so the entire plasma is effectively “frozen in” to the field. A complete description of this effect is not found until section 3.2. Particles also experience a retarding pressure force when traveling up pressure gradients:

$$\mathbf{F}_{pressure} = -\nabla p \quad (3)$$

The pressure force describes collisions between particles of the same species (i.e., electron-electron collisions). Likewise, the viscosity of the plasma also describes a retarding force due to collisions between particles of the same species. It acts to slow adjacent parcels of fluid that are moving with a large velocity shear (i.e., they are moving at different speeds or in opposite directions). The force due to viscosity is expressible in terms of a Maxwell stress tensor:

$$\mathbf{F}_{viscosity} = -\nabla \cdot \tilde{\pi} \quad (4)$$

The fourth and final force describes the effect of collisions between ions and electrons. Called the resistivity of a plasma, this force can be obtained by considering the integrated effect of the electron-ion collision frequency, a derivation of which can be found in most basic plasma physics books (Chen, 1983; Miyamoto, 1980; Goldston and Rutherford, 1995; Krall and Trivelpiece, 1973):

$$\mathbf{F}_{resistivity} = m_e n \langle \nu_{collision} \rangle (\mathbf{v}_i - \mathbf{v}_e) = \eta e^2 n^2 (\mathbf{v}_i - \mathbf{v}_e) \quad (5)$$

where η is called the resistivity. The resistivity describes a momentum transfer between the ions and the electrons of a plasma. Thus, the force is negative for the ions and positive for the electrons. The forms of the pressure and resistivity forces used here ignore any non-isotropic effects.

Now, the sum of these forces yields two equations of motion for the electrons and ions:

$$ma = \sum F \quad (6)$$

$$m_i n_i \frac{d\mathbf{v}_i}{dt} = m_i n_i \left(\frac{\partial \mathbf{v}_i}{\partial t} + (\mathbf{v}_i \cdot \nabla) \mathbf{v}_i \right) = +en_i(\mathbf{E} + \mathbf{v}_i \times \mathbf{B}) - \nabla p_i - \nabla \cdot \tilde{\pi}_i - \eta e^2 n_i^2 (\mathbf{v}_i - \mathbf{v}_e) \quad (7)$$

$$m_e n_e \frac{d\mathbf{v}_e}{dt} = m_e n_e \left(\frac{\partial \mathbf{v}_e}{\partial t} + (\mathbf{v}_e \cdot \nabla) \mathbf{v}_e \right) = \underbrace{-en_e(\mathbf{E} + \mathbf{v}_e \times \mathbf{B})}_{\text{Lorentz Force}} - \underbrace{\nabla p_e}_{\text{Pressure}} - \underbrace{\nabla \cdot \tilde{\pi}_e}_{\text{Viscosity}} + \underbrace{\eta e^2 n_e^2 (\mathbf{v}_i - \mathbf{v}_e)}_{\text{Resistivity}} \quad (8)$$

These equations contain a complete description of the plasma dynamics. The time derivative on the left side is expanded using the convective derivative, $(\mathbf{v}_e \cdot \nabla) \mathbf{v}_e$. The quantities \mathbf{v}_i and \mathbf{v}_e are difficult to measure experimentally. It is much easier to experimentally measure the bulk flow of the plasma and relative velocity of the ions and electrons (the current). To put equations (7) and (8) in these terms, a few assumptions and approximations need to be made. The first assumption is that the plasma is in a quasi-static equilibrium so that the densities of ions and electrons are uniform and $n_i \approx n_e$. Secondly, the ion velocities in quasi-static equilibrium are slow enough that the ion velocity represents the bulk flow of the entire magnetofluid ($\mathbf{v} \approx \mathbf{v}_i$). In this approximation, the ions can be considered stationary with respect to the electrons which have much lower mass and travel at high velocities as they orbit the field lines.

Now, introducing an expression for the current,

$$\mathbf{J} = -en(\mathbf{v}_e - \mathbf{v}_i) \quad (9)$$

we can manipulate the equations of motion (7) and (8) to write the generalized form of Ohm's law:

$$\mathbf{E} + \mathbf{v} \times \mathbf{B} = \underbrace{\eta \mathbf{J}}_{\text{Resistivity}} + \underbrace{\frac{1}{en} \mathbf{J} \times \mathbf{B}}_{\text{Hall Term}} - \underbrace{\frac{1}{en} \nabla p_e}_{\text{Pressure}} + \underbrace{\frac{m_e}{e^2 n} \frac{\partial \mathbf{J}}{\partial t}}_{e^- \text{ Inertia}} \quad (10)$$

A derivation of this can be found in appendix A. The viscosity term $\nabla \cdot \tilde{\pi}$ has been neglected (see appendix A for details). All the other essential elements of the equations of motion in (7) and (8) appear in this equation. It is easy to identify the resistive term $\eta \mathbf{J}$, the pressure term ∇p_e and the Lorentz force $\mathbf{J} \times \mathbf{B}$ which is now called the Hall force. The $m_e \partial \mathbf{J} / \partial t$ term is called the electron inertia term, as is suggested by its form.

3.1 The Magnetic Induction Equation

Ohm's law contains the dynamics of the plasma in terms which can be experimentally measured or manipulated using Maxwell's equations. Various approximations to Ohm's law trade complexity for insight into the plasma dynamics. A simple limiting case is when the

plasma is very dense. With $1/n \rightarrow 0$, everything on the right hand side of Ohm's law (10) is insignificant compared to the resistivity of the plasma. Ohm's law therefore reduces to:

$$\mathbf{E} + \mathbf{v} \times \mathbf{B} = \eta \mathbf{J} \quad (11)$$

This approximation gives us the resistive MHD equation. Maxwell's equations allow us to manipulate Ohm's law:

$$\nabla \cdot \mathbf{E} = \frac{\rho}{\epsilon_0} \quad (\text{Gauss's law}) \quad (12)$$

$$\nabla \cdot \mathbf{B} = 0 \quad (\text{no magnetic monopoles}) \quad (13)$$

$$\nabla \times \mathbf{B} = \mu_0 \mathbf{J} \quad (\text{Ampere's law}) \quad (14)$$

$$\nabla \times \mathbf{E} = -\frac{\partial \mathbf{B}}{\partial t} \quad (\text{Faraday's law}) \quad (15)$$

We can ignore the displacement current term in Ampere's law (14) because it is much smaller than the current term for plasmas for low frequency phenomena. The ratio of the current to the displacement current is:

$$\frac{\mu_0 \mathbf{J}}{\mu_0 \epsilon_0 \frac{\partial \mathbf{E}}{\partial t}} \simeq \frac{\mu_0 \mathbf{J} \tau}{\mu_0 \epsilon_0 (\eta \mathbf{J})} = \frac{c^2 \mu_0 \tau L^2}{L^2 \eta} = \frac{\tau}{\tau_{light}^2} \frac{\mu_0 L^2}{\eta} = \frac{\tau \tau_{diffusion}}{\tau_{light}^2} \gg 1 \quad (16)$$

where τ is the time scale of some change in the magnetofluid and L is a scale length. We have also used the purely resistive Ohm's law $\mathbf{E} = \eta \mathbf{J}$ and the approximation $\partial/\partial t \approx 1/\tau$. Even if we choose the fastest possible motion $\tau = \tau_{light}$, the current density remains significantly larger than the displacement current (since typically the time scales are much slower, $\tau \gg \tau_{light}$, then $\tau \tau_{diffusion} / \tau_{light}^2 \gg 1$). Now, it is possible to use Ampere's law (14) without the displacement current to eliminate \mathbf{J} in Ohm's law,

$$\mathbf{E} = -\mathbf{v} \times \mathbf{B} + \frac{\eta}{\mu_0} \nabla \times \mathbf{B} \quad (17)$$

Taking the curl of this equation and using Faraday's law (15) to express the equation entirely in terms of magnetic field yields the resistive magnetic induction equation:

$$\frac{\partial \mathbf{B}}{\partial t} = \underbrace{\nabla \times \mathbf{v} \times \mathbf{B}}_{\text{convection}} + \underbrace{\frac{\eta}{\mu_0} \nabla^2 \mathbf{B}}_{\text{diffusion}} \quad (18)$$

This equation states that the magnetic field at a particular point can change due to the bulk movement of magnetic structures connected to the plasma (convection) or due to a resistive decay of the fields in the plasma (diffusion). Figure 4 depicts the roles of these two terms graphically. The diffusion of magnetic field in the magnetic induction equation is due only to the resistive decay of currents that support the magnetic fields. Other terms in Ohm's law such as electron inertia which we have neglected in this section can provide other mechanisms for magnetic field to change at a point.

$$\frac{\partial \mathbf{B}}{\partial t} = \nabla \times \mathbf{v} \times \mathbf{B} + \frac{\eta}{\mu_0} \nabla^2 \mathbf{B}$$

Figure 4: According to the magnetic induction equation (for resistive MHD), the magnetic field at a point can change by the superposition of movement of the magnetofluid structures (left) or by resistive decay of a stationary magnetofluid (right).

A magnetofluid can be characterized by the ratio of the convection term to the diffusion term:

$$R_m \equiv \left| \frac{\mu_0 \nabla \times \mathbf{v} \times \mathbf{B}}{\eta \nabla^2 \mathbf{B}} \right| \simeq \frac{\mu_0 v (B/L)}{\eta (B/L^2)} = \frac{\mu_0 v L}{\eta} \quad (19)$$

where L and v are characteristic scale length and velocity, respectively and where we have defined a new quantity, the magnetic Reynolds number. If $R_m \gg 1$, then the convective term dominates and the magnetic structures are frozen in to the plasma. Wherever the plasma moves, the magnetic field is dragged along with it. At the other limit, if $R_m \ll 1$, then the plasma behaves like an insulator because it is completely decoupled from the magnetic field and the two diffuse through each other freely.

3.2 Frozen-In Flux Constraint

The simplest limiting case for Ohm's Law is obtained when the resistivity of a plasma goes to zero, leaving the magnetic induction equation (18) with only the convection term:

$$\frac{\partial \mathbf{B}}{\partial t} = \nabla \times \mathbf{v} \times \mathbf{B} \quad (20)$$

The convective term describes how magnetic structures are frozen into the plasma. This can be shown explicitly (Biskamp, 1997) if one calculates the change in flux across a surface $S(t)$ bounded by a curve $\ell(t)$ that moves with the fluid at a velocity \mathbf{v} :

$$\frac{d}{dt} \int_S \mathbf{B} \cdot d\mathbf{a} = \int_S \frac{\partial \mathbf{B}}{\partial t} \cdot d\mathbf{a} + \int_{\frac{\partial S}{\partial t}} \mathbf{B} \cdot d\mathbf{a} \quad \text{by chain rule} \quad (21)$$

$$= \int_S \nabla \times (\mathbf{v} \times \mathbf{B}) \cdot d\mathbf{a} + \int_{\ell} \mathbf{B} \cdot (\mathbf{v} \times d\boldsymbol{\ell}) \quad \text{see figure 5} \quad (22)$$

$$= \int_{\ell} (\mathbf{v} \times \mathbf{B}) \cdot d\boldsymbol{\ell} + \int_{\ell} \mathbf{B} \cdot (\mathbf{v} \times d\boldsymbol{\ell}) \quad \text{by Stoke's theorem} \quad (23)$$

$$= \int_{\ell} (\mathbf{v} \times \mathbf{B}) \cdot d\boldsymbol{\ell} - \int_{\ell} (\mathbf{v} \times \mathbf{B}) \cdot d\boldsymbol{\ell} = 0 \quad \text{by vector identities} \quad (24)$$

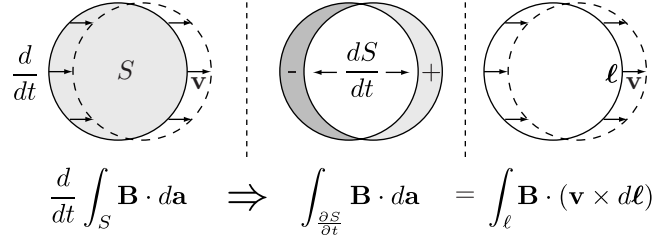


Figure 5: Illustration of the step to get equation 22 in the calculation of the frozen-in flux constraint.

where we have used the steps indicated and the triple product identity:

$$\mathbf{A} \cdot (\mathbf{B} \times \mathbf{C}) = \mathbf{C} \cdot (\mathbf{A} \times \mathbf{B}) = (\mathbf{A} \times \mathbf{B}) \cdot \mathbf{C} = -(\mathbf{B} \times \mathbf{A}) \cdot \mathbf{C} \quad (25)$$

$$\mathbf{B} \cdot (\mathbf{v} \times d\boldsymbol{\ell}) = -(\mathbf{v} \times \mathbf{B}) \cdot d\boldsymbol{\ell} \quad (26)$$

The boundary line ℓ encircling \mathbf{B} defines a flux tube where the amount of flux contained in the tube is constant. As the diameter of S goes to zero, the flux tube becomes a field line (Biskamp, 1997). Flux is conserved in these tubes of plasma and the same topological structure of field lines or flux tubes will remain no matter how convoluted they may become as they follow the plasma motion. The flux is therefore said to be frozen into the plasma.

4 Reconnection Theory

Magnetic reconnection is the topological rearrangement of field lines as magnetofluids with opposing magnetic field come in contact. The reconnection *layer* is the region where the topological rearrangement occurs. If two flux surfaces are pushed up against each other, then the plane in which the oppositely oriented magnetic field vectors lie is called the reconnection *plane*.

Two adjacent bundles of magnetofluid with oppositely oriented field lines create a sheet of current (by Ampere's law) along the reconnection layer and normal to the reconnection plane. If there were no resistivity, the flux bundles could get very close, creating infinitely thin and strong current sheets. In the limit of low resistivity ($\eta \rightarrow 0$) and neglecting all other terms in the generalized Ohm's law, we are left with only a convective component term in the magnetic induction equation:

$$\frac{\partial \mathbf{B}}{\partial t} = \nabla \times \mathbf{v} \times \mathbf{B} \quad (27)$$

This equation provides no mechanism for field lines to rearrange themselves with respect to the plasma. The flux bundles can move into convoluted shapes with filamental sheet currents running throughout and never experience any topological rearrangement of field lines.

The terms on the right-hand side of Ohm's law allow the fields to move with respect to the plasma. In the general case Ohm's law is

$$\mathbf{E} + \mathbf{v} \times \mathbf{B} = \mathbf{R} \quad (28)$$

where \mathbf{R} is a generalized force field. In the resistive MHD approximation, $\mathbf{R} = \eta \mathbf{J}$, yielding the magnetic induction equation. The Sweet-Parker model is based on a purely resistive Ohm's law and assumes that the fluid is incompressible. In the general case, however, we have

$$\mathbf{R} = \eta \mathbf{J} + \frac{1}{en} \mathbf{J} \times \mathbf{B} - \frac{1}{en} \nabla p_e + \frac{m_e}{e^2 n} \frac{\partial \mathbf{J}}{\partial t} \quad (29)$$

These additional terms provide other mechanisms for the plasma to diffuse across field lines and are especially significant for reconnection processes observed for plasmas where the resistivity is low. Such a collisionless theory, proposed by Biskamp, Drake, Shay and others, has a more complicated structure and requires numerical simulations to verify.

4.1 Incompressible Fluid Model (Sweet-Parker)

The Sweet-Parker model (Sweet, 1958; Parker, 1957) describes a system in equilibrium where the magnetofluid convecting into the reconnection region is exactly balanced by the diffusion of magnetic field at the reconnection point. The magnetic Reynolds number for the system (the ratio of convection to diffusion) is therefore exactly 1. Figure 6 shows two parcels of magnetofluid with oppositely oriented magnetic field being merged at a velocity v_{in} . At their intersection, a boundary layer of thickness 2δ is formed where the opposing flux is annihilated. Integrating Ampere's Law around this boundary layer (or take the curl at any point in the layer) shows that there is a current sheet pointing out of the page. If there

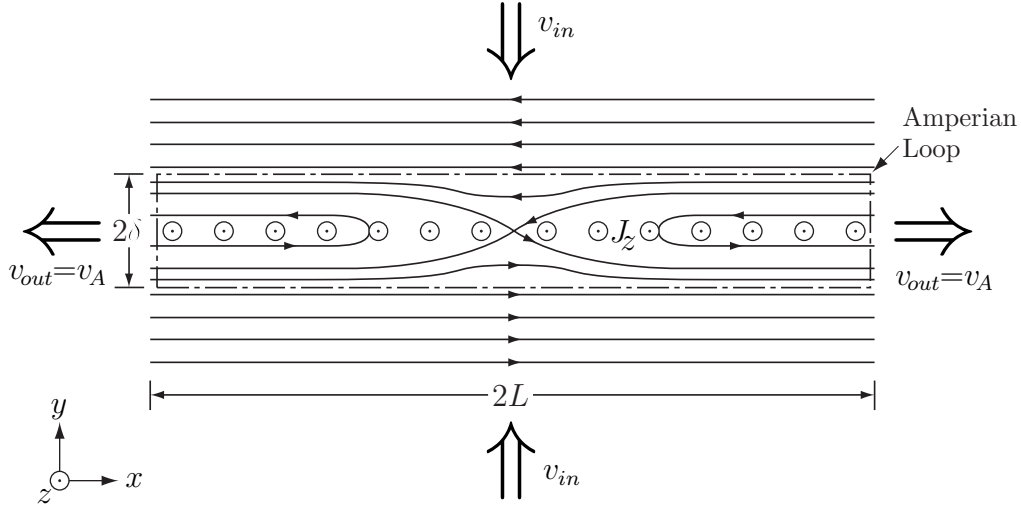


Figure 6: Schematic of the magnetic field configuration for the reconnection layer. Two parcels of magnetofluid with oppositely oriented magnetic field merge at inflow velocity v_{in} . A current sheet J_z develops at the reconnection layer. Magnetofluid is accelerated to the Alfvén velocity as reconnected field lines relax.

were no resistivity, the current sheet could hold off an infinitely thin boundary layer. Finite resistivity, however, prevents this situation and bundles of magnetic flux can flow across the boundary layer and annihilate with a corresponding bundle of flux with oppositely oriented field. The annihilation of flux in this model is merely due to the resistive diffusion of magnetic field.

The derivation of the model proceeds as follows. Assuming incompressibility, the amount of fluid going in is equal to the amount of fluid going out:

$$\delta v_{out} = L v_{in} \quad (30)$$

We want this model to make a prediction about the thickness of the reconnection layer 2δ given a scale length of the system $2L$. The unknown quantities are the velocities. The outflow velocity is easy: the inflowing magnetofluids have oppositely oriented magnetic flux which annihilate in the reconnection layer. The outflow plasma has no magnetic field, so conservation of energy demands that the magnetic energy in the magnetic fields that reconnect annihilate and get converted into the kinetic energy of the particles.

$$\frac{1}{2} \rho v^2 = \frac{B_x^2}{2\mu_0} \quad (31)$$

$$v_{out} = v_{Alf} \equiv \frac{B_x}{\sqrt{\rho\mu_0}} \quad (32)$$

The resulting outflow velocity is called the Alfvén speed and is represented by v_{Alf} . This is the maximum speed at which a kink in a magnetofluid can straighten itself out. Now, we seek an expression for the last remaining variable, the inflow velocity v_{in} . Outside the layer, the magnetic field is completely uniform and straight so by Ampere’s law, there is no curl

in the magnetic field and therefore no current flowing. Ohm's law outside the layer where no current flows can be written:

$$E_z + v_{in}B_x = 0 \quad \text{Ohm's law outside layer} \quad (33)$$

Two more expressions to eliminate E_z and B_x are provided by using Ampere's law around the perimeter of the layer and Ohm's law inside the layer. Inside the layer, the flow slows to a standstill before being accelerated out the sides. There is a curl in the magnetic field along the reconnection layer which produces a current sheet J_z . Taking an Amperian loop around the reconnection layer, as shown in figure 6, we pick up $(4L)B_x$ on the horizontal paths and no contribution on the vertical parts where $\mathbf{B} \perp d\boldsymbol{\ell}$. The loop surrounds a current $J_z(\text{Area}) = J_z(2L2\delta)$. The result from Ampere's law is therefore:

$$4LB_x = \mu_0 J(2L2\delta) \quad \text{Ampere's law around layer} \quad (34)$$

Ohm's law inside the layer includes the current, but there is no velocity since the flow stagnates before being accelerated out at the edges:

$$E_z = \eta J_z \quad \text{Ohm's law inside layer} \quad (35)$$

The assumption that the system is steady state means that $d\mathbf{B}/dt = 0$ and by Faraday's law, $d\mathbf{B}/dt = \nabla \times \mathbf{E} = 0$, so the electric field \mathbf{E} must be uniform everywhere. Thus, we may equate the electric field E_z inside and outside the layer. We are now able to solve for the inflow velocity by taking equation (33) and substituting the expressions for E_z (35) and B_x (34) to get:

$$v_{in} = \frac{E_z}{B_x} = \frac{\eta J_z}{\mu_0 J_z \delta} = \frac{\eta}{\mu_0 \delta} \quad (36)$$

Returning to (30) and inserting the expressions for the inflow velocity (36) and the (Alfvénic) outflow velocity (32) we have the equation:

$$\delta \left(\frac{B_x}{\sqrt{\rho \mu_0}} \right) = L \left(\frac{\eta}{\mu_0 \delta} \right) \quad (37)$$

This can be solved for the dimensionless quantity δ/L that describes the width of the reconnection layer and current sheet, yielding:

$$\frac{\delta}{L} = \frac{1}{\sqrt{S}} \quad (38)$$

where S is the Lundquist number, which is just the magnetic Reynolds number with $v = v_{Alf}$. The total width of the layer is:

$$\delta_{S-P} \equiv 2\delta = \frac{2L}{\sqrt{S}} \quad (39)$$

Introducing the notation for the total scale length $L' = 2L$:

$$\delta_{S-P} = \frac{L'}{2\sqrt{S}} \approx 0.15 \text{ cm} \quad (40)$$

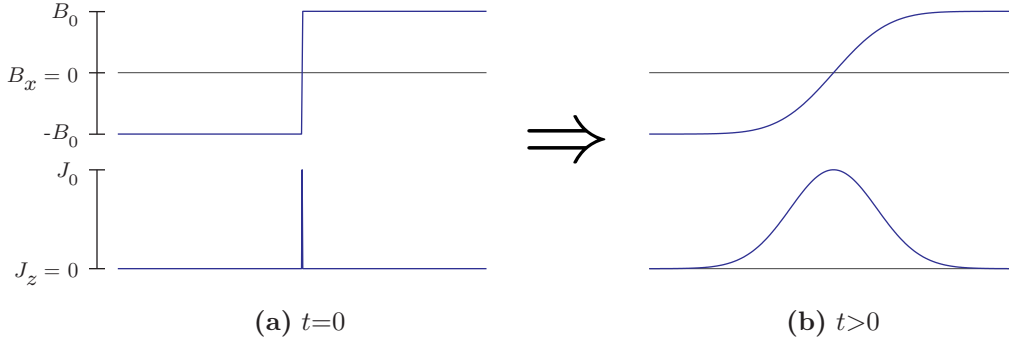


Figure 7: Magnetic field and current profiles showing evolution of an infinitely thin current sheet according to the magnetic diffusion equation. At $t = 0$ in (a) the system is in equilibrium with step function in B_x and a delta function in J_z . A time $t > 0$ later in (b) the field and current profiles evolve to an error function and a Gaussian, respectively.

For SSX plasmas $S \approx 1000$ and using $L' = 10$ cm, the width of the layer is $\delta_{S-P} = 0.15$ cm.

The profiles of the magnetic field and current sheet along the y axis can be found using simple arguments (Parker, 1994). Consider a field configuration similar to the one shown in figure 6, although for the moment the resistivity has been removed so that the magnetic field is uniformly $B_x = +B_0$ in $y > 0$ and $B_x = -B_0$ in $y < 0$ with a infinitely thin discontinuity. Taking the magnetic field profile to be a step function, the current sheet must be a delta function at $y = 0$. These profiles are plotted in figure 7a. At time $t = 0$ the magnetofluid is given a small, uniform resistivity η . The system evolves according to the magnetic induction equation (18):

$$\frac{\partial B_x}{\partial t} = \frac{\eta}{\mu_0} \frac{\partial^2 B_x}{\partial y^2} \quad (41)$$

The convection term drops out because the system is steady state so that $\mathbf{v} = 0$. This equation can be solved explicitly:

$$B_x = B_0 \operatorname{erf} \left(\frac{y}{\sqrt{4\eta t}} \right) \quad (42)$$

where erf is the error function

$$\operatorname{erf}(\chi) = \frac{2}{\sqrt{\pi}} \int_0^\chi e^{-s^2} ds \quad (43)$$

The shape of the error function is very similar to \tan^{-1} which is easier to fit to the magnetic profile data. The profile of the current sheet is given by Ampere's law to be the derivative of error function, or a Gaussian:

$$J_z = \frac{\partial B_x}{\partial y} = \frac{B_0}{\mu_0 \sqrt{\pi \eta t}} \exp \left(-\frac{y^2}{4\eta t} \right) \quad (44)$$

These time-evolved profiles are plotted in figure 7b. The profiles spread out with time although the spread slows down according to $\sqrt{4\eta t}$. In the Sweet-Parker reconnection model

presented above, the thickness of this layer is determined by the balance of the diffusive spreading and the convective inflow. In the steady state, the magnetic profiles that are measured in the experiment should fit to an error function. The exact scaling, as we shall see, may be strongly influenced by parameters in Ohm's law that have been excluded from the Sweet-Parker model.

4.2 Collisionless Reconnection (Biskamp and Drake)

The Sweet-Parker model predicts that the thickness of the layer vanishes with $1/\sqrt{S}$ and thus predicts a very thin boundary layer for high Lundquist number plasmas. However, it has been experimentally observed at SSX that the reconnection layer remains macroscopically wide even in the collisionless limit of small resistivity η . These observations motivate a theory that retains more terms in the expression for Ohm's law. The model in this section is proposed by Biskamp et al. (1997) and elaborated upon by Shay et al. (1997). Henceforth, this theory will be referred to as the collisionless reconnection model.

The general form for Ohm's law (10) is repeated here:

$$\mathbf{E} + \mathbf{v} \times \mathbf{B} = \eta \mathbf{J} + \frac{1}{en} \mathbf{J} \times \mathbf{B} - \frac{1}{en} \nabla p_e + \frac{m_e}{e^2 n} \frac{\partial \mathbf{J}}{\partial t} \quad (45)$$

We are interested in how much each term contributes to the total dynamics of the plasma. To compare the contribution of each term, we introduce the following normalizations so that all the terms in the equation become dimensionless:

$$\hat{v} = \frac{v}{v_{AIf}}, \quad \hat{\mathbf{B}} = \frac{\mathbf{B}}{B_0}, \quad \hat{t} = \frac{t}{\tau_{AIf}}, \quad \hat{\nabla} = L \nabla \quad (46)$$

where L is a characteristic scale length and τ_{AIf} is the transit time for something traveling that length at the Alfvén speed. Dimensionless current density and the electric field are obtained from Ampere's law and Faraday's law, respectively:

$$\hat{\mathbf{J}} = \frac{\mu_0 L}{B_0} \mathbf{J}, \quad \hat{\mathbf{E}} = \frac{\tau_{AIf}}{B_0 L} \mathbf{E} \quad (47)$$

Substituting these normalizations into Ohm's law produces an apparently messy situation (which is not dimensionless, either):

$$\frac{B_0 L}{\tau_{AIf}} \hat{\mathbf{E}} + v_{AIf} B_0 \hat{\mathbf{v}}_i \times \hat{\mathbf{B}} = \frac{\eta B_0}{\mu_0 L} \hat{\mathbf{J}} + \frac{B_0^2}{en \mu_0 L} \hat{\mathbf{J}} \times \hat{\mathbf{B}} - \frac{1}{en L} \hat{\nabla} p_e + \frac{m_e B_0}{e^2 n \tau_{AIf} \mu_0 L} \frac{\partial \hat{\mathbf{J}}}{\partial \hat{t}} \quad (48)$$

Fortunately, these simplify upon dividing through by $B_0 v_{AIf}$ to make the equation dimensionless and replacing bunches of constants by dimensionless plasma parameters and length ratios:

$$\hat{\mathbf{E}} + \hat{\mathbf{v}}_i \times \hat{\mathbf{B}} = \frac{1}{S} \hat{\mathbf{J}} + \frac{\delta_i}{L} \hat{\mathbf{J}} \times \hat{\mathbf{B}} - \frac{\delta_i}{L} \beta \hat{\nabla} p_e + \left(\frac{\delta_e}{L} \right)^2 \frac{\partial \hat{\mathbf{J}}}{\partial \hat{t}} \quad (49)$$

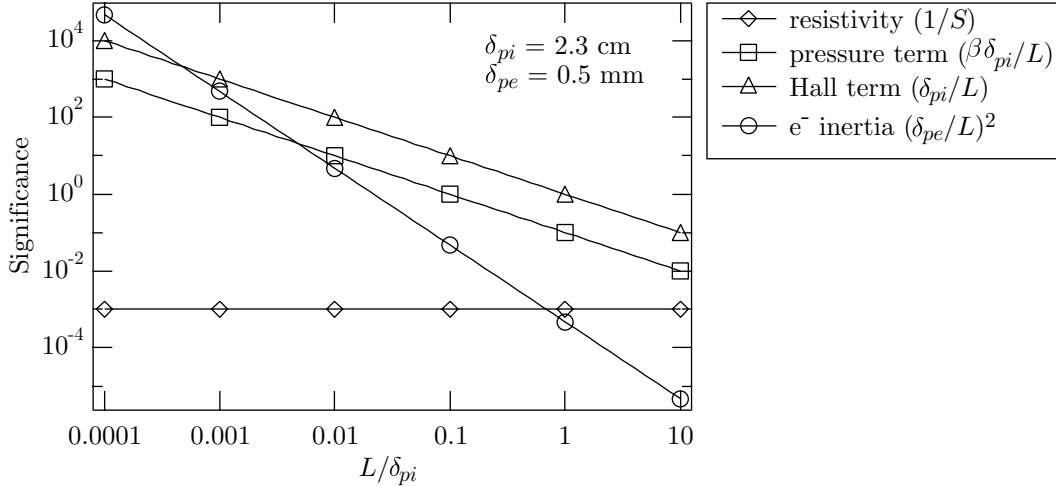


Figure 8: The scaling of the four terms on the right of the dimensionless Ohm's law equation (49). Plotted are the dimensionless scaling factors in front of each term as a function of the scale length, L over which we are interested. For small scales $L/\delta_{pi} \leq 10^{-4}$, the electron inertia term dominates. For sufficiently large scales, the resistivity wins out. In the middle, pressure and Hall terms dominate.

where δ_i and δ_e are the ion and electron inertial lengths, respectively. They are defined as follows:

$$\delta_{i,e} \equiv c/\omega_{pi,pe}, \quad \omega_{pi,pe} \equiv \sqrt{\frac{m_{i,e}\epsilon_0}{ne^2}} \quad (50)$$

These quantities are fundamental values for a plasma; they describe the distance over which the ion and electron have significant inertial effects. The term $\omega_{pe}/2\pi$ is often called the plasma frequency, or the frequency below which electromagnetic waves are not able to propagate (and are reflected) due to induced electron motion. If the frequency of the wave is higher than the plasma frequency, then the electrons are too slow to respond to a fast changing electromagnetic field and allow the electromagnetic wave to pass through the plasma. Likewise, the scale length c/ω_{pe} describes the scale below which an electron cannot respond to a rapid *spatial* change in the field. If a magnetic field has curves on a scale well above c/ω_{pe} , then the electron will follow those contours as it orbits a field line. If, however, the field has wiggles of characteristic scale less than c/ω_{pe} , the electron is unable to remain frozen to the field because its inertia is a significant factor in its motion at these small scales. An identical description of the quantity c/ω_{pi} can be made for ions.

Returning to the normalized generalized Ohm's law, we are now able to compare the coefficients of each dimensionless term to see how much each of the terms contributes to the motion of the plasma. The relative value of each of the four coefficients on the right hand side of equation (49) is plotted in figure 8. The variable in this plot is the characteristic scale length that we are interested in. For very large scales ($L \gg c/\omega_{pi}$), every term except for the resistivity becomes insignificant, indicating that resistive MHD models are good for large scale magnetofluid motion.

When the scale length is on the order of $L \lesssim c/\omega_{pi}$, the Hall and pressure terms

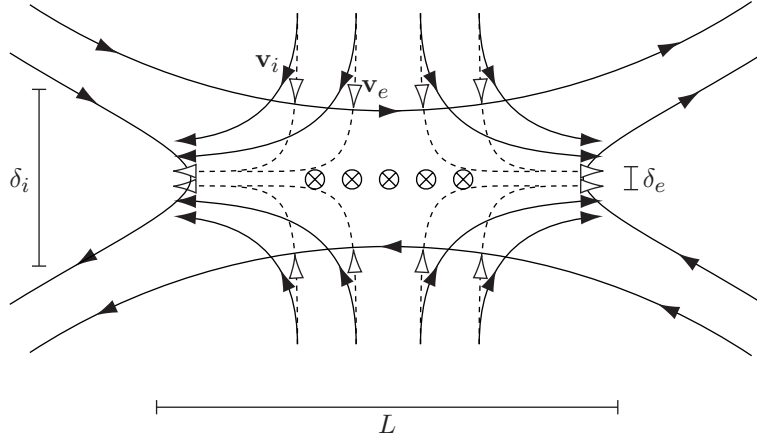


Figure 9: Structure of the collisionless reconnection layer according to the collisionless reconnection model. Ions must turn the corner at a much larger scale $\delta_i \propto c/\omega_{pi}$ than the electrons due to their large inertia.

begin to dominate. The Hall term allows ions to decouple from the electrons. Under Hall dynamics, the ions flow at a slower rate than the electrons and thereby create a current. The current points antiparallel to the inflowing electrons and perpendicular to the \mathbf{B} field. Thus, the $\mathbf{J} \times \mathbf{B}$ force of the Hall term points out of the plane, creating a weak ion current out of the plane. In other words, the Hall term allows there to be differential flow of the ions with respect to the electrons only if the ions also move out of the plane. The electrons remain frozen into the field lines in this regime since they have much less inertia and are more strongly influenced by the magnetic fields on these scales.

On the scale of the electron inertial length $L \lesssim c/\omega_{pe}$, the frozen-in flux constraint is broken and reconnection can occur. The exact mechanism for reconnection is unknown, though the breaking of the frozen-in flux constraint means that the fields are free to rearrange and reconnect themselves on that scale. There is a very thin and strong current sheet in the layer according to Ampere's law, just as in the Sweet-Parker sheet. The electrons are accelerated out of this very narrow reconnection layer by a mechanism that converts magnetic energy into kinetic energy. Since the magnetic energy is only accelerating the electrons and not the ions on this scale, we expect them to reach super-Alfvénic speeds. As the electrons are accelerated away from the ions, an electric field is established, pulling the ions in towards the reconnection layer and then out towards the outflow. As the ions are accelerated by the electrons, the electrons slow down considerably. Although the electrons may be temporarily accelerated to super-Alfvénic speeds in the reconnection layer, energy balance dictates that the final velocity of ions and electrons out of the reconnection region must be Alfvénic. Figure 9 contains an illustration of this complex model.

The magnetic field profiles change with the out-of-plane current. All the fields reconnect on the scale of c/ω_{pe} ; thus, one might expect the profile to be no wider than c/ω_{pe} . Despite the high current density on the c/ω_{pe} scale, the small total area over which the current density exists makes the total out-of-plane current contribution insignificant. The ion current density is much lower than the electron current density, but the ion current density exists over a much larger area (on the scale of c/ω_{pi} which is $\gg c/\omega_{pe}$). Because of ion

current density exists over a much larger area than the electron current density, the total contribution of the ion current density to the out-of-plane current is much more significant than the electron contribution. The field profiles therefore change on the scale of c/ω_{pi} .

These analytical arguments are supported by the results from numerical simulations by Shay et al. (1997). A two fluid plasma is simulated in two dimensions as it undergoes reconnection. The ions are modeled as particles because they develop multiple beams (jets). The electrons are modeled as a fluid. As predicted, the ions decouple from the electrons at a distance of c/ω_{pi} from the reconnection layer. Since there are ions flowing in from both sides, the total width of the layer will be two ion inertial lengths:

$$\delta_C = 2c/\omega_{pi} \quad (51)$$

This distance will be called the ‘‘collisionless thickness’’. Likewise, the electrons turn towards the outflow at a distance of c/ω_{pe} from the neutral line and then accelerate outward. The peak outflow velocity of the electrons exceeds the Alfvén velocity because the electrons are no longer coupled with the ions. The out-of-plane differential flow between the electrons and ions produces the expected scaling of the magnetic field.

The numerical simulations of this theory also show a number of new features. The electron flows on the c/ω_{pe} scale produce a standing whistler wave² that propagates outward along the magnetic field from the X-point. The whistler wave creates a strong electric field at the reconnection layer that accelerates the electrons to the high outflow velocity, which also has the effect of dragging the magnetic field out of the plane. As described above, the Hall term $\mathbf{J} \times \mathbf{B}$ causes the ions to decouple from the electrons and drift towards the reconnection layer. As the electrons move rapidly away from the reconnection region, the electric field created between the separated species makes the ions turn the corner and accelerates them to near-Alfvénic velocities at the outflow. By varying the temperature of the plasma, the simulations also showed that the reconnection layer scales were unaffected, ruling out any theory that states that the width of the layer is proportional to the Larmor radius ρ_i .

In summary, the Hall term allows ions to decouple from electrons. The out-of-plane ion flow causes the magnetic field to change on the c/ω_{pi} scale. On the c/ω_{pe} scale, the electron inertia breaks the frozen-in constraint and a standing whistler wave accelerates electrons out of the reconnection region to super-Alfvénic velocities. Because the ions are much more massive than the electrons, the ions and electrons separate, which creates electric fields that accelerate ions toward the reconnection layer and the outflow.

4.3 Turbulent Reconnection Layers (Matthaeus)

Turbulence is often ignored in analytical models and computational simulations of magnetic plasmas because it is assumed to have a small, perturbative effect. Matthaeus et al. (1984) demonstrated the significance of turbulence by running simulations that produce magnetic field O-points due to turbulence in the reconnection layer. An O-point is shown in figure

²In the simplest approximation, a whistler wave is a wave that propagates along magnetic field lines like Alfvén waves, but is so fast that the ions can be considered stationary with respect to the electrons, which move and oscillate with the field. They exhibit nonlinear effects and can propagate at angles to magnetic field contours.

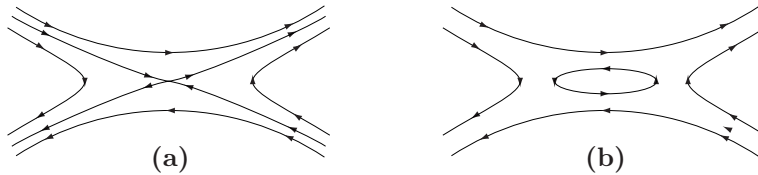


Figure 10: Magnetic field structure for (a) an X-point and (b) an O-point.

10b. Since the plasma is confined to move along field lines, the circular fields in the O-point trap the plasma. The protons and electrons are accelerated by the reconnection electric field to very high velocities out of the plane. Particles near an X-point, on the other hand, are quickly moved away by reconnecting field lines. They do not have as much time to be accelerated by the out-of-plane electric field.

Matthaeus' simulations are performed using purely resistive MHD for plasmas with Reynolds numbers equal to 1000. In this way, the simulated plasma is similar to SSX plasmas. The data are represented in Fourier space, which allows for finer and more accurate structures to develop since it treats both large and small scale interactions with equal accuracy. This is particularly important at the reconnection layer where the relevant processes occur on both the microscopic and macroscopic scales.

The simulations are set up with periodic boundary conditions and alternating bands of oppositely oriented magnetic field. This creates two current sheets at the two intersections of the magnetic field bands. Turbulence is created by adding at the beginning a small random broadband perturbation to the fields. Test particles are introduced into the magnetofluid and their paths are traced by plotting their motion under the Lorentz force (1) as the magnetofluid evolves.

The simulations show that magnetic O-points, dubbed “magnetic bubbles”, form at the reconnection layer, trapping a small number of particles. These particles become accelerated out of the plane due to the reconnection electric field. This is the same field that supports the current sheets, but since ions are now trapped in the reconnection region, they can be significantly accelerated. Thus, the magnetic bubbles create an ion beam out one side of the reconnection plane and an electron beam out the other side. The ions are accelerated to well over 1600 times their original energy and up to 80 times the Alfvén speed (Ambrosiano et al., 1988). These simulations are performed with magnetic Reynolds number ≈ 1000 , similar to plasmas created in SSX. Thus, these results can be experimentally tested in SSX by looking for very high energy particles normal to the layer of reconnection. The size of the magnetic bubbles is macroscopic and might be observable with the magnetic probe resolution available to SSX. Yamada et al. (1997) has observed O-points when merging two spheromaks in certain configurations. These O-points may be the result of turbulence in the reconnection region, although more simulation and experimentation are required to verify this claim.

5 Spheromak Plasmas

A spheromak is a toroidal ring of plasma in equilibrium according to basic MHD equations of motion; it is a good source of stable magnetofluid for reconnection experiments. The plasma contains helical currents and magnetic fields that are continuous around the toroid. Figure 11 shows the magnetic fields decomposed into the poloidal and toroidal components. The toroidal field runs the long way around the toroid and the poloidal field runs the short way around the ring. Although they are not drawn in this figure, the current that generates these fields is also helical.

The magnetic fields confine the plasma according to the frozen-in flux constraint, but if there were nothing to contain the magnetic field, the spheromak would expand infinitely just as a puff of gas in a vacuum does. SSX uses a copper cylinder “flux conserver” to contain the magnetic fields. As the field encounters the copper wall, image currents flow in the copper according to Faraday’s law and prevent the magnetic field from passing through the wall.

SSX uses magnetized coaxial plasma guns to create spheromaks. The schematic in figure 12 shows how the formation process works. A puff of gas is introduced into the annular gap between the inner and outer coaxial cylindrical electrodes (figure 12a). High voltage capacitors charged to 5 kV are connected to the electrodes and cause the gas to ionize and become a toroid of plasma. Current flowing in the gun and through the plasma interacts with its own magnetic field to produce a $\mathbf{J} \times \mathbf{B}$ force which accelerates the plasma towards the open end of the gun (figure 12b). The same acceleration mechanism is found in a typical rail gun. A strong magnetic field, called the “stuffing field”, is produced by an external magnetic coil and is concentrated in the center electrode with a slug of high permittivity metal. The plasma encounters this magnetic field at the opening of the gun and resists the change in field according to Faraday’s law. Because plasma is an excellent conductor, currents flow in the toroid of plasma as the it distends the stuffing field (figure 12c). If the magnetic pressure from the gun exceeds the magnetic tension of the stuffing field, the toroid breaks away to form a spheromak. The field lines distend and then reconnect in back as the spheromak forms. The Spheromak inherits toroidal field from the gun field and poloidal field from the stuffing field (figure 12d). The process is analogous to blowing a soap bubble. The soap film tension represents the stuffing field strength and the pressure of one’s breath represents the magnetic pressure of the gun current. A soap bubble is formed when the breath’s pressure overcomes the surface tension of the soap. The amount of gun current (breath) required to overcome the stuffing field (soap film) is called the formation threshold. Appendix C is devoted to the detailed study (by the author) of the formation threshold for coaxial plasma guns.

After formation, the spheromak is not in equilibrium with the field, pressure and current profiles imposed by the coaxial plasma gun. Reconnection allows the fields to rearrange themselves towards a minimum energy state. The equilibrium of a spheromak is essentially the lowest energy configuration of the magnetic fields with pressure forces on the plasma. The simplest equation of equilibrium is obtained by balancing of magnetic (Lorentz) and pressure forces (following Geddes, 1997):

$$\nabla p = \mathbf{J} \times \mathbf{B} \tag{52}$$

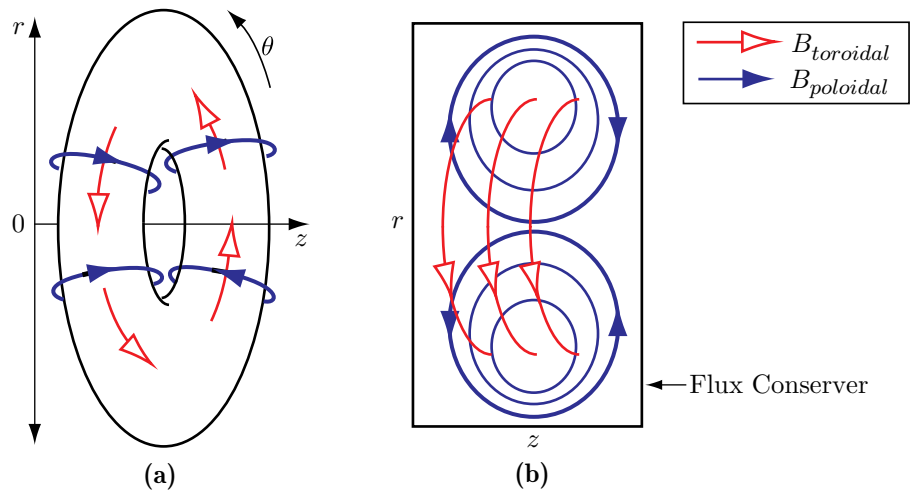


Figure 11: A spheromak is a toroid of magnetofluid with helical fields which can be decomposed into poloidal and toroidal fields as shown.

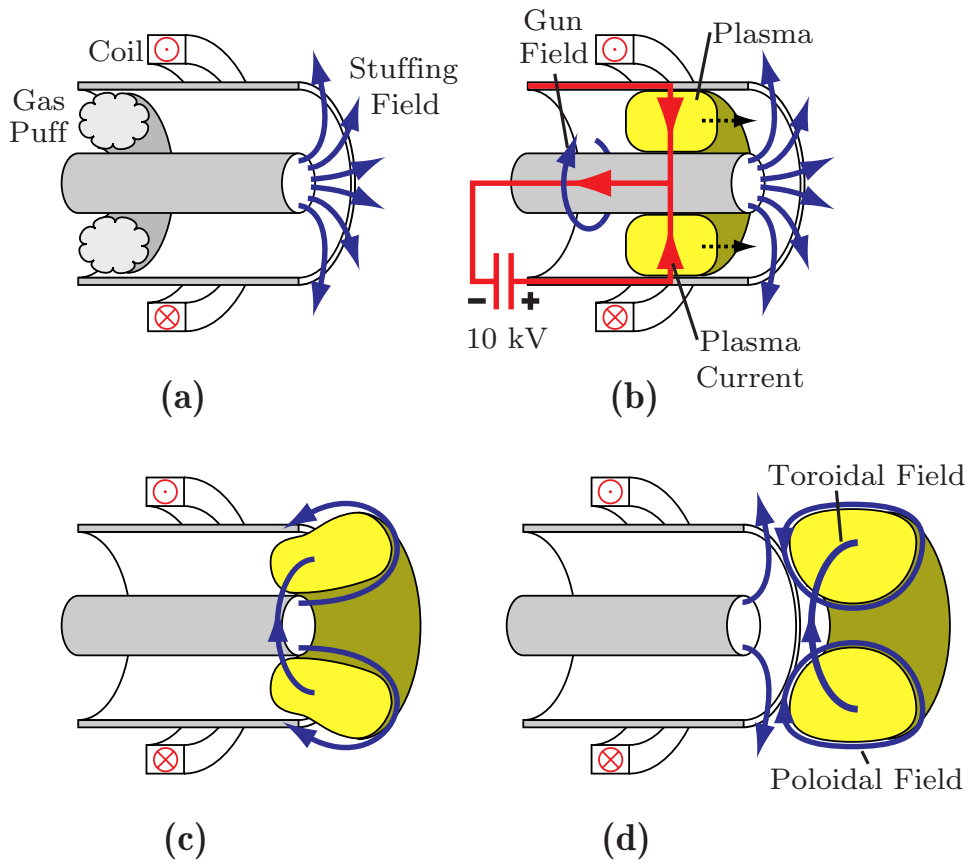


Figure 12: Formation of a spheromak using a magnetized coaxial plasma gun. See text for details.

Since spheromaks are characterized by low β (or the ratio of kinetic to magnetic pressure) kinetic pressure effects can be neglected by setting $\nabla p \rightarrow 0$. Now, by Ampere's law, $\mathbf{J} \propto \nabla \times \mathbf{B}$ and so the equation can be written entirely in terms of the magnetic field:

$$0 = (\nabla \times \mathbf{B}) \times \mathbf{B} \quad (53)$$

This equation implies that $\nabla \times \mathbf{B} \parallel \mathbf{B}$, which can be rewritten as

$$\nabla \times \mathbf{B} = \lambda_{eq} \mathbf{B} \quad (54)$$

where λ_{eq} can be a constant or a function of flux. Solutions of constant lambda in a cylindrical boundary condition yield good first order approximations to the structure of a spheromak (Taylor, 1986; Schaffer, 1987). Equilibrium studies on SSX (Geddes et al., 1998) have shown that non-constant lambda solutions are necessary to account for the magnetic profiles at certain times in the spheromak's lifetime.

6 Experimental Setup

The SSX reconnection experiments use spheromaks as reservoirs of stable magnetofluid for reconnection processes. Two spheromaks are held in adjacent flux conservers with two symmetrical chevron-shaped cutouts so that they can interact and reconnect. The flux conservers are 2.5 cm apart so that any products of reconnecting magnetofluid can be detected using particle detectors and x-ray detectors on the periphery of the machine directed at the reconnection region.

The spheromak is a good choice as a source of magnetofluid because it is easy to make with coaxial plasma guns, simple to handle with copper flux conservers, and has naturally strong magnetic fields. It is also characterized by low β which indicates that the plasma dynamics are not strongly affected by pressure. Because it is unlinked, the spheromak can be created at the ends of the vacuum chamber and then translated to the region in the center where the experiment takes place. This freedom allows the sources of electromagnetic noise in the spheromak formation regions to be removed from the experiment. Spheromak plasmas are also similar to solar flares in exhibiting low β and high temperature. Therefore, magnetic reconnection studies using spheromaks can be directly applied to solar physics.

Figure 13 shows a picture of the lab. The experiment takes place in the 1 m diameter vacuum chamber at the center of the picture. A cutaway of the vacuum chamber and its contents is shown in figure 14. The vacuum chamber contains two flux conservers of radius $r_{cons} = 25.4$ cm and length $L_{cons} = 30.8$ cm. Two coaxial magnetized plasma guns of radius $r_{gun} = 8.41$ cm are built into the endcaps of the vacuum chamber and form spheromaks into the flux conservers. The spheromaks communicate across a 2.5 cm gap via large 10 cm by 5 cm chevron-shaped slots cut out of the back of each flux conserver. The chevrons are wide enough for the magnetofluid to flow through the gap, yet are small enough for the spheromak to be held in place by the remainder of the flux conserver. If the back walls were completely removed, the spheromaks would be susceptible to tilt instabilities. The chevrons also define a localized area in which the reconnection occurs so that the detectors need only measure in one place. If there were no copper walls, reconnection would still occur but the newly reconnected plasma would still be frozen into the plasma. The resistive walls allow fields lines to end on the walls so that particles accelerated by reconnection will be free in the gap between the flux conservers. The gap design is therefore essential to the detection of directional jets of ions.

The coaxial plasma guns can create left- or right-handed spheromaks by switching the polarity on the stuffing field magnet. The handedness of a spheromak is defined by which hand is used to describe the direction of the field lines if the thumb points along the toroidal field and the the curled fingers point in the direction of the poloidal field. Merging spheromaks of opposite handedness, also called counter-helicity merging, creates a reconnection layer with parallel but opposite magnetic fields. Figure 15 shows the two possible configurations of counter-helicity merging which create reconnection planes in two different directions. If the particle detector (labeled ‘RGEA’ and discussed below in section 6.2) is placed to look along the reconnection plane of one configuration, then it looks normal to the layer of the other configuration.

Magnetic probes are inserted into the plasma to measure the magnetic field in the reconnection region simultaneously with the particle flux. Low and high resolution linear

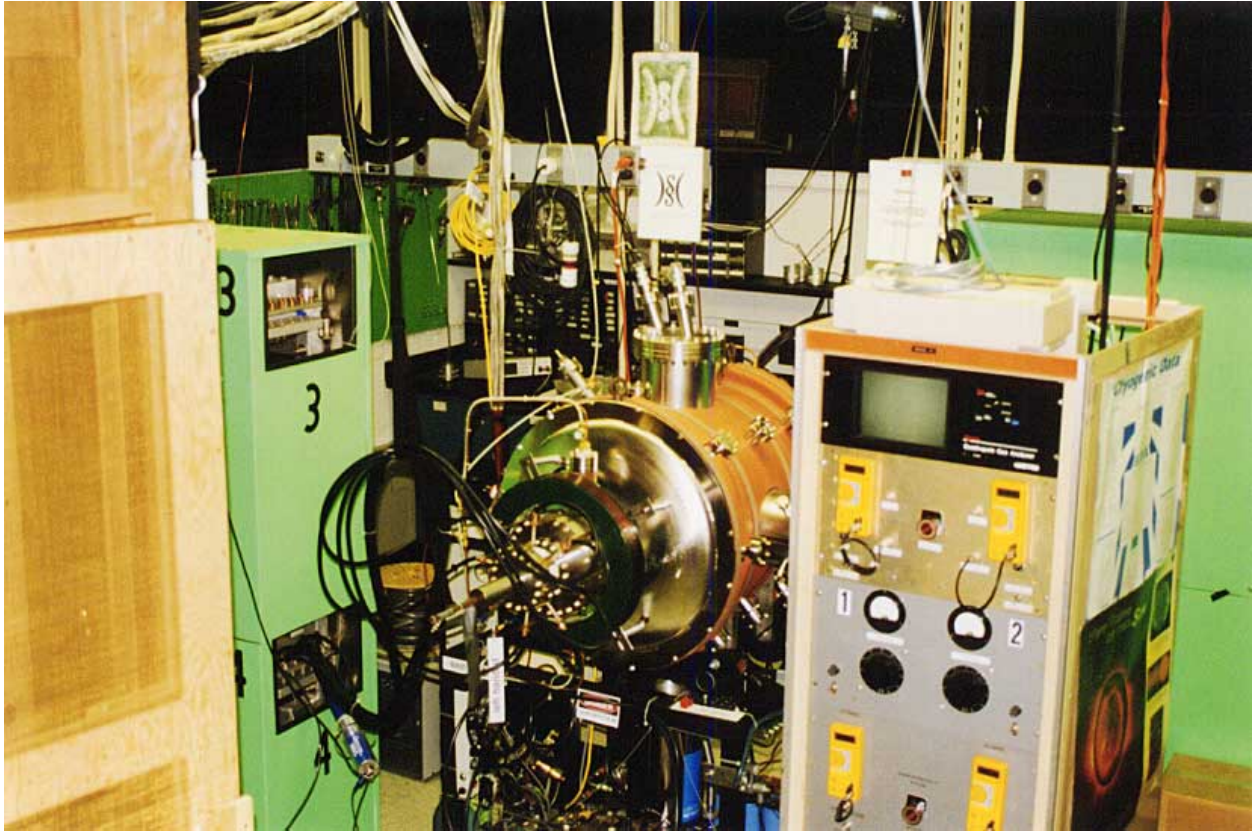


Figure 13: View of the lab showing the Faraday cage on the far left and the vacuum chamber in the center. The large (green) boxes house the high voltage capacitors.

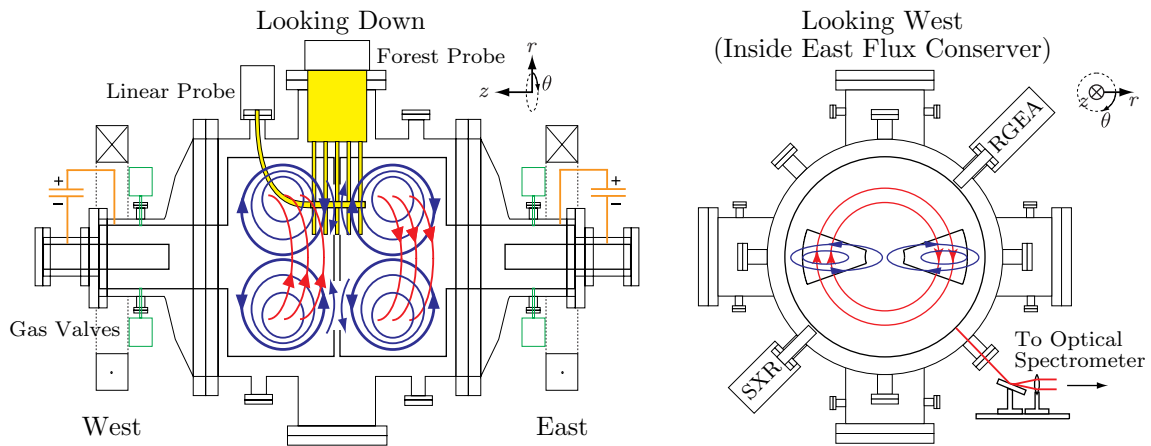


Figure 14: Cutaway view of the SSX apparatus with coaxial magnetized plasma guns at either end. The spheromaks are injected into the flux conservers which have symmetrical chevron-shaped holes cut out so that the spheromaks touch. Particle detectors look down the gap between the two flux conservers at the reconnection region. Also shown are the positions of the magnetic probes.

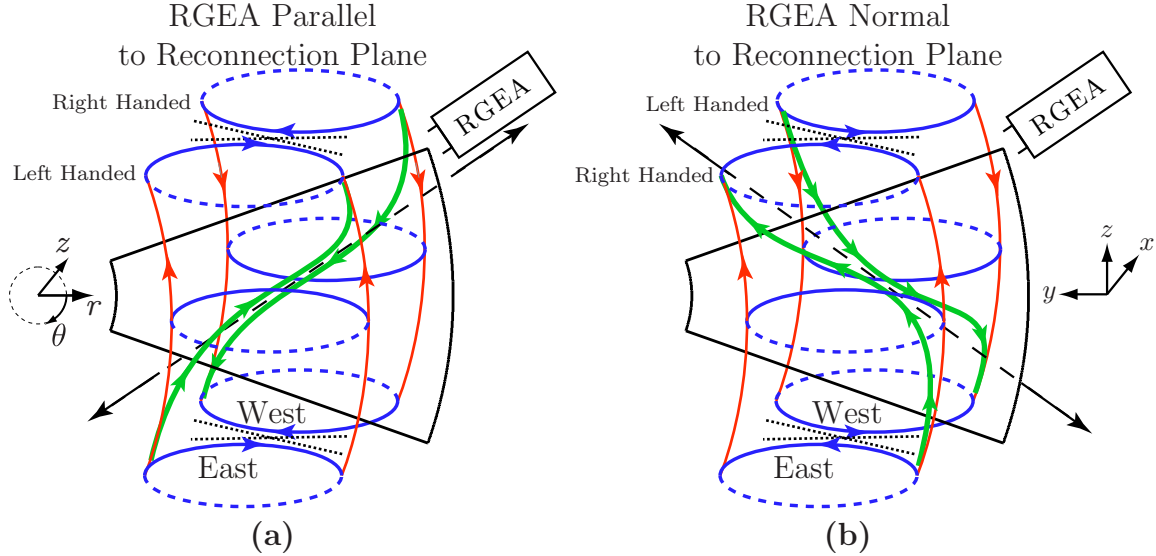


Figure 15: Opposite helicity spheromaks can create a reconnection layer oriented in two possible directions. (a) shows an east spheromak with left handed helicity and a west spheromak with right handed helicity such that the retarding grid energy analyzer (RGEA) is in the reconnection plane. Swapping the helicities of the two spheromaks in (b) puts the RGEA approximately normal to the reconnection plane.

probes measure magnetic field along a line that passes directly through and perpendicular to the reconnection layer as shown in figure 16. The forest probe measures a 2D 5 by 6 map of the magnetic field in the reconnection layer and is positioned as shown in figure 17. The extra probe housings will be used in a future experiment to create a 3D map of the magnetic field in the reconnection region. Both probe housings are shown in figure 14, though only one is inserted at a time. More on the magnetic probes can be found in the next section (6.1).

The present experiment uses two Northstar Research capacitive power supplies, one connected to each gun, that are each capable of delivering 25 kJ of energy over about 25 μ s. A separate system supplies power to an electromagnetic coil to create up to 3.7 mWb of “Stuffing Flux” through the gun. Typical gun parameters are 1.5 mWb of Stuffing Flux, 5 kV charge on capacitors and 100 kA peak current (6 kJ of energy). The power supplies appear as the large green boxes in figure 13.

Figure 18 shows one of four gas valves that were custom designed by the author for use on SSX. Each delivers a volume $\approx 0.5 \text{ cm}^3 \text{ H}_2$ at 1 atm per pulse. A pair is connected to each coaxial plasma gun and introduce a total of volume $\approx 1 \text{ cm}^3 \text{ H}_2$ at 1 atm per pulse into the gun in annular region between the electrodes. This volume corresponds to a maximum particle inventory of $N \leq 10^{18}$ ions or electrons per spheromak. A summary of the gas valve design is presented in appendix D.

Triple probe measurements (Ji et al., 1991) yield $T_e \approx 20 \text{ eV}$ and $n_e \approx 10^{14} \text{ cm}^{-3}$ for SSX data. The triple probe data are presented in appendix B. The average magnetic field is 500 G. These values give $c/\omega_{pi} \approx 2 \text{ cm}$ and $S \lesssim 1000$ and predict a resistive reconnection layer thickness $\delta < 1 \text{ cm}$. The collisional mean free path is $\approx 10 \text{ cm}$ and the Alfvén speed is

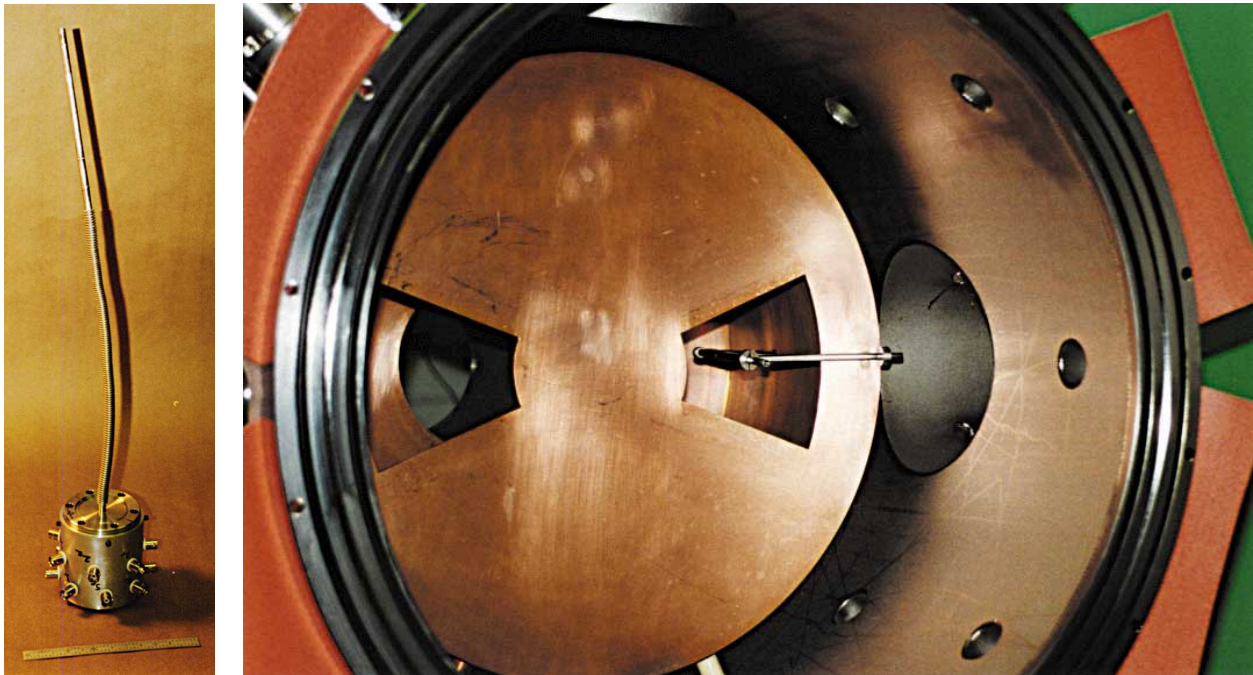


Figure 16: The flexible linear probe before and after installation in the west flux conserver.

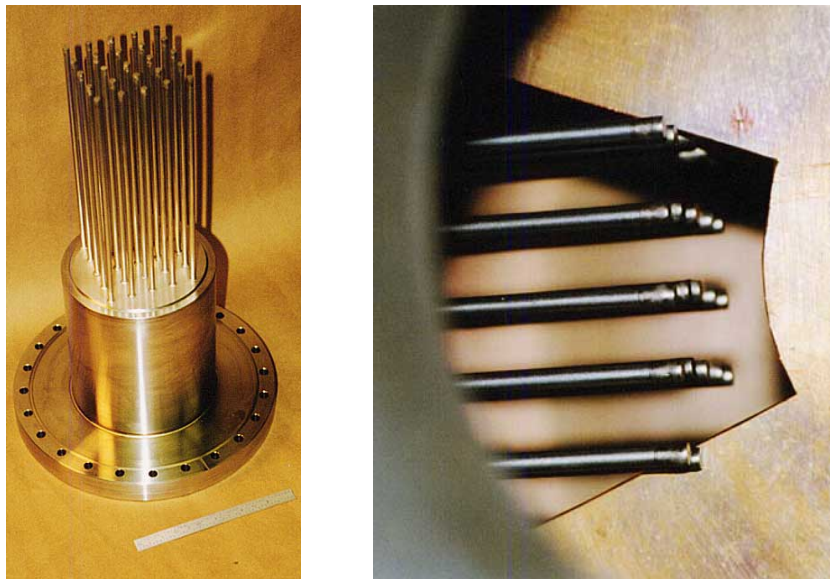


Figure 17: The forest probe before and after installation. Installed photo was taken inside the flux conserver through the outer electrode of the west coaxial plasma gun.

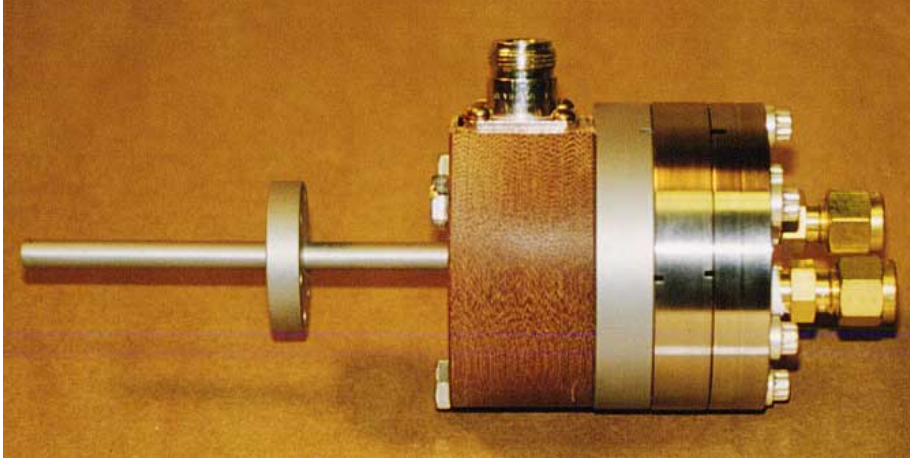


Figure 18: The Kornack valve, a fast (300 μs open time) gas valve.

about 10^7 cm/s. These and other plasma parameters are summarized in table 1.

6.1 Magnetic Probes

Magnetic probes, consisting of small coils of magnet wire, measure all three orthogonal components of the plasma's magnetic field. These 3-coil sets are wound on a flexible teflon or rigid delrin rod before being wrapped in teflon tape and inserted into a vacuum welded, thin wall stainless steel casing, as shown in figure 19.

The linear magnetic probes measure profiles of the magnetic field through the reconnection region. Pictures of the linear probe housing and its placement in the machine are shown in figure 16. The low resolution linear magnetic probe measures all three components of \mathbf{B} at 5 locations separated by 2 cm. The high resolution linear probe has twice as many coil sets at half the separation distance. Both of the linear probes have a teflon coil form so that the probe is flexible. The stainless steel casing is made of 0.12 mm wall 304 stainless steel, which is a non-magnetic and high resistance metal. The time for flux to soak through the tube is short ($\tau_{soak} \leq 0.1 \mu\text{s}$) compared to the time scales of relevant processes and

| | | |
|-------------------------|-------------------|---------------------------|
| density | $n_e \approx n_i$ | 10^{14} cm^{-3} |
| temperature | $T_e \approx T_i$ | 20 eV |
| magnetic field | $B_{typical}$ | 500 G (1000 G max.) |
| Beta | β | 10% |
| Alfvén speed | v_{Alf} | 10 cm/ μs |
| Lundquist Number | S | $\lesssim 1000$ |
| electron skin depth | c/ω_{pe} | 0.5 mm |
| ion skin depth | c/ω_{pi} | 2.3 cm |
| Larmour radius | ρ_i | 0.9 cm |
| Sweet-Parker thickness | δ_{S-P} | 0.15 cm ($L' = 10$ cm) |
| collisionless thickness | δ_C | 4.6 cm |

Table 1: SSX Plasma Parameters

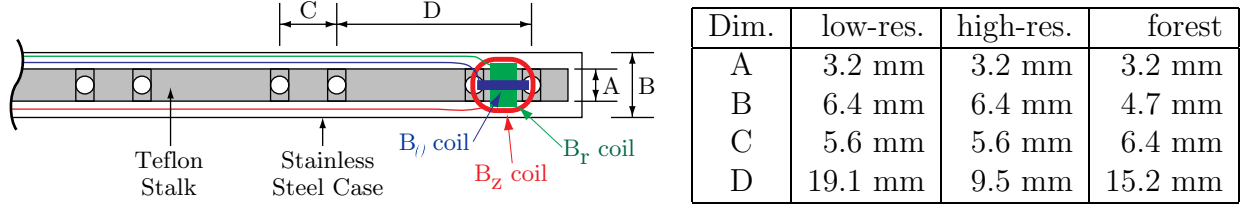


Figure 19: The magnetic probe design. The high resolution version has half the probe separation distance. Dimensions change slightly for the forest probe which has a 4.7 mm stainless steel casing and more closely spaced coil sets. The forest probe also fewer turns per coil.

therefore should not affect the probes significantly.

The forest probe currently measures a 2D map of the magnetic field in the reconnection region. Pictures of the forest probe housing and its placement in the machine are shown in figure 16. It consists of 25 separate stainless steel tubes and delrin magnetic probe coil forms, manufactured according to the specifications in figure 19. The 25 stainless steel tubes are spaced 19.1 mm apart on a square grid. For the current experiments, only five of the tubes are filled with probes to measure a 2D map of the magnetic field through the center of the reconnection region. The 2D map consists of 6 points spaced 15.2 mm apart radially (along r) and 5 points spaced 19.1 mm apart axially (along z). The low resolution linear probe was designed and built by Cameron Geddes; the high resolution linear probe and the forest probe were designed and built by the author.

When the magnetic field changes through a coil of magnet wire, a voltage is produced in the wire according to Faraday's law:

$$V = \frac{d\Phi}{dt} = NA \frac{dB_{\perp}}{dt} \quad (55)$$

The voltages measured by digitizers must therefore be integrated and calibrated to retrieve B . The calibration of the coils in the linear probes is accomplished using a Helmholtz coil that produces a known magnetic field:

$$B = \frac{N\mu_0 I}{2a} \left(\frac{4}{5}\right)^{3/2} \quad (56)$$

where N is the total number of turns, a is the radius of the coil, and I is the current through the loop. The coil is placed in the field and the field is pulsed. The position and orientation of the coil are adjusted until the coil produces the maximum signal, ensuring that the coil is orthogonal to the field. The signal from the probe is passed through the entire data processing system so that any variation in the cabling, filtering, digitizing or integration is calibrated out. The ratio of the magnetic field intensity to the integrated coil signal provides a calibration constant for each coil. Even if this calibration process is accomplished for each coil, there is a chance that the teflon/delrin rod may be twisted. The twist is usually uniform so the resulting magnetic field vectors are simply rotated about the probe axis. There is also a chance that the coils may not be completely orthogonal to one another and would therefore exhibit signal crosstalk. The crosstalk was measured for a sample of coil sets and was found to be much less than 5 percent of the total signal.

The calibration of the forest probe is also accomplished by pulsing a known magnetic field through the probe. Instead of performing the calibration on each probe coil individually, a large Helmholtz coil was built to fit around all 25 probe stalks so that all the coils that measure along a particular axis could be calibrated simultaneously. Only three calibration pulses, one for each axis, are required to calibrate the entire probe. Since the Helmholtz coil is not centered on the probe coils, the actual magnetic field at each coil location was obtained by numerically integrating the Biot-Savart Law.

The signal passes through either coaxial cable or triple-shielded twisted pair bundles into a Faraday cage where the data acquisition and signal processing take place. It is then sent through a 10 MHz RC low pass filter to eliminate high frequency noise before being digitized. SSX uses DSP 2028 CAMAC digitizers that sample at 10 MHz with 8-bit resolution over a range of 5 V or more. The signals are numerically integrated in the processing code. The low resolution of these digitizers causes the signal to be rounded up or down to the nearest value on the 8-bit scale. These rounding errors propagate through numerical integration and makes the integral level out at some nonzero value when the flux disappears. These integrals are corrected by eliminating any zero-offset level from the signal before the experiment and then forcing the integral to return to zero after the signal disappears and the experiment is over. A correction is then applied to the rest of the signal to make it fit these conditions. This method has been verified by numerically integrating a digitizer with a higher (16-bit) resolution and faster sampling rate (50 MHz).

The presence of stainless steel magnetic probes in the plasma will disturb the plasma. Experiments show, however, that the effect is minimal. Small “nub” probes, which extended past the edge of the flux conserver by just 7 mm, measured the magnetic field at the edge of the flux conserver. A linear probe was then inserted through the spheromak in place of one of the nubs. The lifetime of the spheromak was unchanged and the magnitudes of the fields were the same within the usual run to run variation.

6.2 Retarding Grid Energy Analyzer

The Retarding Grid Energy Analyzer (RGEA), designed by Peter Sollins, selectively measures ion flux of energy greater than a chosen value. The designs follow from previous work on energy analyzers by Leal-Quiros and Prelas (1988) and Simpson (1961). A schematic of the detector is shown in figure 20 with a plot of the electric potential through the detector. In these experiments, the RGEA sits outside the flux conservers (about 50 cm away) and looks between them so that it measures only the particles escaping the reconnection layer. The device includes two fine stainless steel screens that are held at negative and positive voltages to repel electrons and ions, respectively. The outermost screen is connected to the copper casing and is held constant at -10 V to eliminate most of the electrons from the incoming flux. The inner screen has a variable positive voltage that can be set to repel ions of energy lower than the voltage of the screen. Those ions with sufficiently high energy make it past the second retarding screen and move directly into the collector cup which is strongly negatively biased. The current is converted to a voltage using a known resistor. The voltage is measured by an oscilloscope and serves as an arbitrary unit of incoming particle flux. The only signal processing applied to these data is a numerical low pass filter to eliminate high frequency noise.

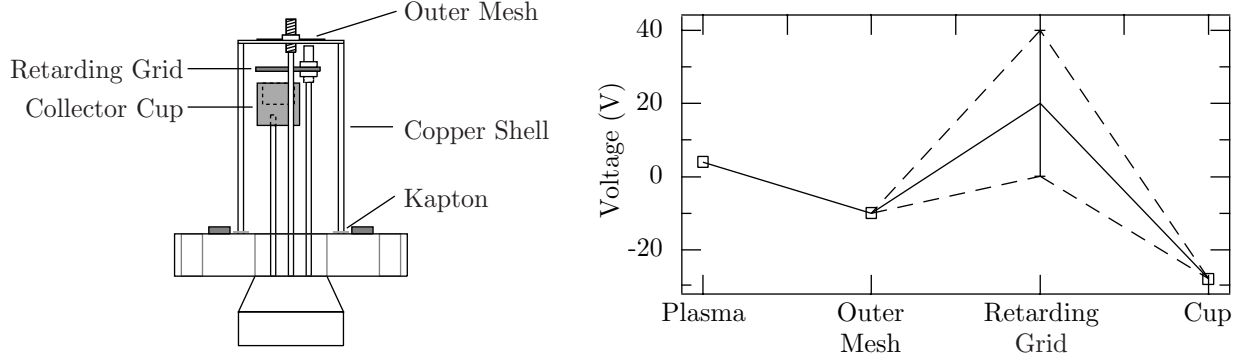


Figure 20: Schematic of the Retarding Grid Energy Analyzer (RGEA). Electrons are repelled by the negative outer shell. Positive ions with sufficient energy to pass through the retarding grid are measured by the collection cup.

The average energy of the ion flux can be determined by sweeping the retarding grid voltage to get an energy spectrum of the ion beam. If we assume a thermal distribution (more on this in the results section), then the analysis is straightforward. A thermal Maxwell distribution can be written as:

$$f(v) = \left(\frac{m}{2\pi kT}\right)^{3/2} n \exp\left(-\frac{mv^2}{2kT}\right) \quad (57)$$

Rewriting the velocity and the temperature in terms of energies ($K = mv^2/2$ and $\bar{E} = 1/kT$), we no longer have to deal with a Gaussian:

$$f(v) = \underbrace{n \left(\frac{m}{2\pi}\right)^{3/2}}_C \bar{E}^{-3/2} \exp(-K/\bar{E}) \quad (58)$$

The RGEA detects all those particles with energy greater than energy eV_0 where V_0 is the voltage on the retarding grid. The total signal is therefore given by:

$$S(V_0) = C\bar{E}^{-3/2} \int_{eV_0}^{\infty} \exp(-K/\bar{E}) dK \quad (59)$$

$$= C\bar{E}^{-3/2} (\bar{E} \exp(-K/\bar{E})|_{eV_0}^{\infty}) \quad (60)$$

$$= \frac{C}{\sqrt{\bar{E}}} \exp(-eV_0/\bar{E}) \quad (61)$$

Thus, to find the temperature of a experimentally measured spectrum, we simply fit the data to the form

$$\Gamma = \Gamma_0 \exp(-V_0/\bar{E}) \quad (62)$$

where the average energy \bar{E} and Γ_0 are the fit parameters.

7 Experimental Results

The spheromaks created in SSX are free to move around the flux conserver and exhibit dynamic and unrepeatable behavior from run to run. For this reason, all magnetic data are recorded during the same run. Equilibrium studies on SSX (Geddes et al., 1998) yielded important information about the evolution of spheromaks in SSX. The time history of each run can be broken into three major sections: formation, relaxation, and equilibrium. When the spheromaks first exit the guns, they are traveling at the Alfvén speed due to the strong $\mathbf{J} \times \mathbf{B}$ acceleration through the Stuffing Field. They are timed to hit the back walls of the flux conservers simultaneously at around $t = 25 \mu\text{s}$. Their large initial velocity causes the spheromaks to bounce off the back walls once or twice before becoming stationary. At $t = 40 \mu\text{s}$, although the spheromak is relatively stationary in the flux conserver, it remains in a non-equilibrium field configuration since the poloidal and toroidal fields have approximately the same magnitude at the edge. For $t > 50 \mu\text{s}$, the spheromak has settled into a force free state of equilibrium. Each phase of the spheromak evolution has different effects on the magnetic reconnection processes. The initial, high velocity merging of the two spheromaks drives the reconnection. The subsequent equilibrium state should resemble a more idealized equilibrium model like the ones that were discussed in the theory section.

This section will present the data from the linear and 2D magnetic probe arrays and the energetic particle detector (RGEA). The magnetic profiles and energy time series and spectra will be compared to theoretical predictions.

7.1 Linear Probe Results

A typical experimental run is shown in figures 21 and 22. For this run, spheromaks of opposite helicity were arranged so as to put the RGEA in the plane of reconnection. The east spheromak was right handed and the west spheromak was left handed so that the magnetic field vectors lie in a plane that points at the RGEA (corresponding to the configuration shown in figure 15a). The reconnecting field lines accelerate particles towards the RGEA.

For this run, the RGEA was set to repel ions with energy less than 40 eV. Figure 22 contains a plot of the magnetic energy density around the layer (figure 22a) and the signal on the RGEA (figure 22b) for the same run. The magnetic energy density is defined as average magnetic energy density over all the probes:

$$W = \frac{1}{N} \sum_{n=1}^N \frac{B^2}{2\mu_0} \quad (63)$$

where the N is the number of probes (3-coil sets), which for this run, $N = 5$. The RGEA signal is filtered using a low pass filter in order to reduce the noise from the capacitive power supplies that appears at the beginning of the run. The oscillations in signal are an artifact of filtering this noise and are not real. As shown in the unfiltered signal, the noise does not continue appreciatively through the most important part of the data.

As shown in figure 21a, the fields in the gap grow quickly to a maximum near $t_1 = 33 \mu\text{s}$. At this time, shortly after the spheromaks are formed, a reconnection layer has formed with opposed poloidal and toroidal fields. The width of the current sheet is difficult

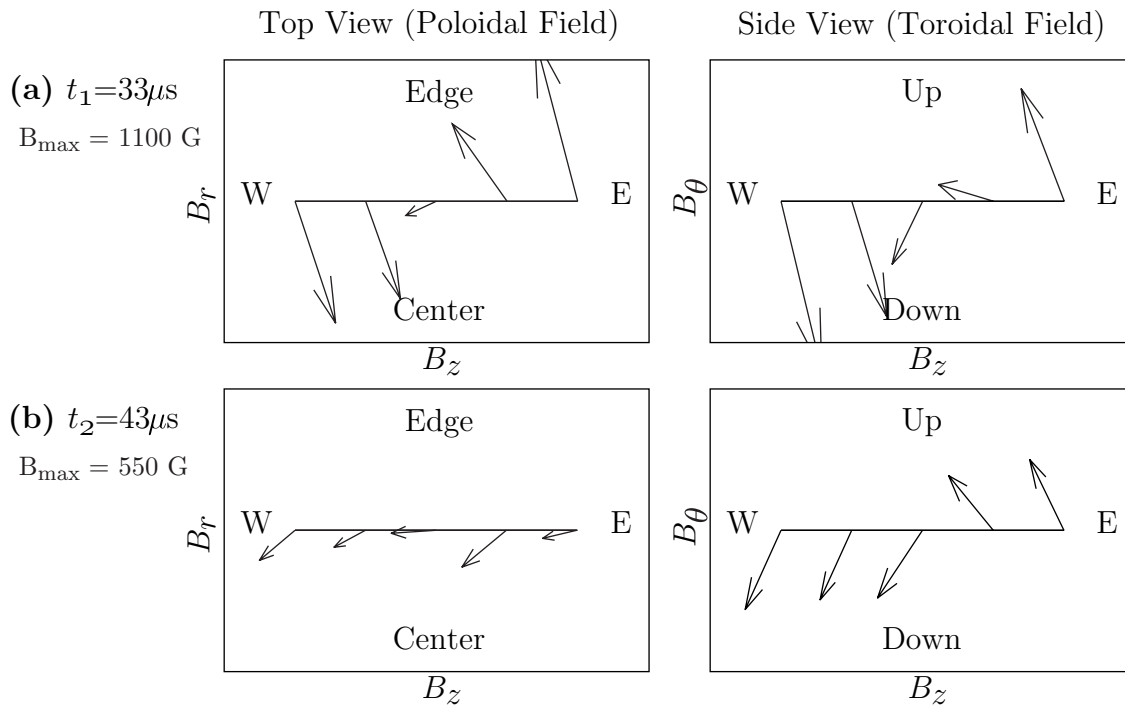


Figure 21: Poloidal and toroidal projections of the magnetic field in the reconnection region at time (a) t_1 before annihilation (b) t_2 after annihilation $10 \mu\text{s}$ later. Probe separation is 2 cm. (Run #13(97/10/8))

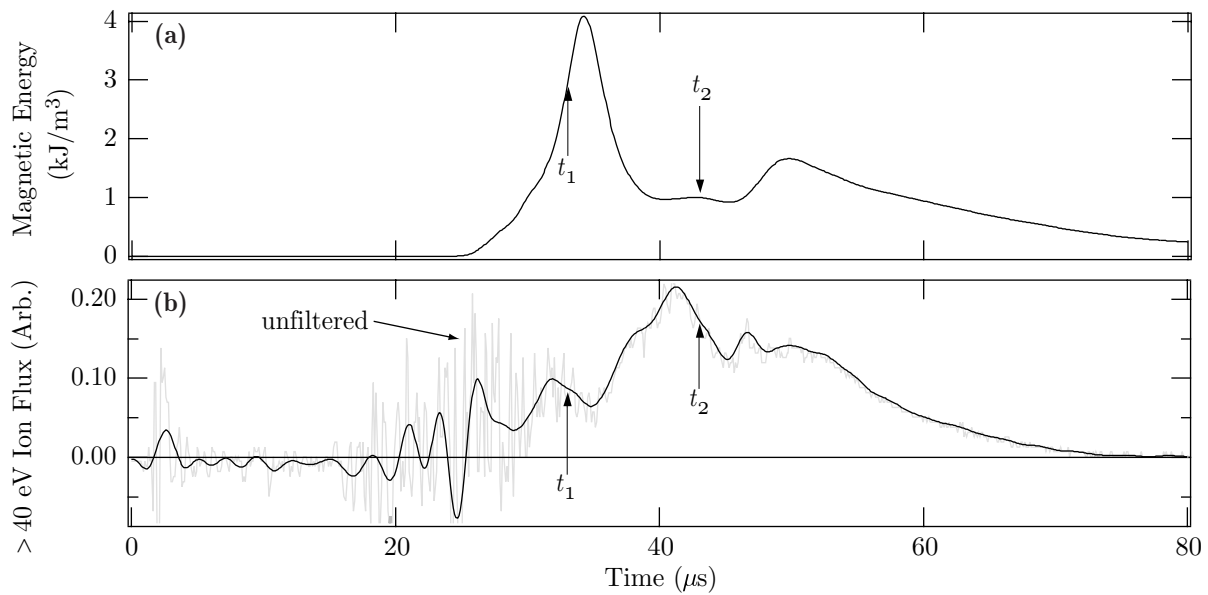


Figure 22: Time history of the run shown in figure 21. Plotted are the (a) local magnetic energy density and (b) energetic ion flux. (Run #13(97/10/8))

to determine due to the coarse spacing of the probes; a higher resolution probe verifies this measurement later. Immediately after the formation of the reconnection layer, the field strengths rapidly decrease, and at $t_2 = 43 \mu\text{s}$ (figure 21b) much of the flux has been annihilated.

Correlated with this flux annihilation event is a burst of plasma flow at the RGEA. This is evident in the timeseries plotted in figure 22. As the two spheromaks initially touch, the magnetic energy density peaks as the reconnection layer is formed. Immediately thereafter, as observed in the field plots, the fields around the reconnection layer quickly decrease. The sharp drop in magnetic energy is followed about $5 \mu\text{s}$ later by a peak in the $\geq 40 \text{ eV}$ ion flux at the RGEA. The velocity of the ion flux traveling a distance of 50 cm to the RGEA in this amount of time is approximately the Alfvén speed of the plasma, $10 \text{ cm}/\mu\text{s}$. These observations constitute the first time that ion jets have been spatially and temporally resolved in a single run. A reconnection experiment by Gekelman et al. (1982) shows similar Alfvénic flow using a highly reproducible plasma and the measurements of a scanned single probe averaged over hundreds of runs. A recent experiment by Ono and Yamada et al. (1996) reports bulk heating from spectral temperature measurements.

To test for out-of-plane accelerated ion flux, the RGEA (still set to repel ions with less than 40 eV) was placed so that it looked normal to the plane of reconnection. The toroidal and poloidal projections of the magnetic fields are shown in figure 23 at two times: $t_1 = 34 \mu\text{s}$ and $t_2 = 41 \mu\text{s}$. As in the previous run, the magnetic fields build up as the spheromaks come together (figure 23a) and then rapidly disappear (figure 23b). Figure 24 shows the particle flux and the average magnetic energy density for the same run. Note that the peak ion flux out of the plane of reconnection is four times smaller than the peak ion flux measured in the plane of reconnection (compare out-of-plane data in figure 22b to in-plane data in figure 24b). The drop in magnetic field after $t_1 = 34 \mu\text{s}$ is followed almost immediately ($\Delta t \approx 1 \mu\text{s}$) by a peak in the energetic ion flux. In fact, the data show that for each of the three peaks in the magnetic field, there are three peaks in the RGEA, offset by $1 \mu\text{s}$. The three peaks may be due to oscillations of the spheromak after its initial impact with the back wall of the flux conserver.

These RGEA measurements constitute preliminary evidence that there is a very small flux of very highly energetic particles traveling normal to the reconnection layer. These observations may be the first verification of the turbulent reconnection simulations by Matthaeus et al. (1984). Note that the magnetic profiles in figure 23a do not have the field reversal point at the same place. The poloidal field reversal moves smoothly in 3 cm to match the position of the toroidal field reversal as shown in figure 23b. There is no clear explanation for the field configuration in figure 23a, demonstrating the need for a full 2D or 3D map of the magnetic field to fully understand the magnetic structure.

The thickness of the reconnection layer has been verified with the high resolution probe array which has twice as many probes in the same space as the probes used in figure 21. Figure 25 shows poloidal field for a run similar to that shown in Figure 23 at $t_1 = 34 \mu\text{s}$. Ampere's law for the profile simplifies to $J_z \sim \partial B_y / \partial x$, which allows one to infer the shape of the current from the magnetic field. As is predicted by the magnetic diffusion equation, the profiles for current and magnetic field fit reasonably well to the Gaussian and error function, respectively. In figure 25a the width at half maximum of the current layer is $\delta \simeq 2 \text{ cm}$, which is smaller than $\delta_C = 2c/\omega_{pi} = 4.6 \text{ cm}$ for our plasma. This is most likely due to the

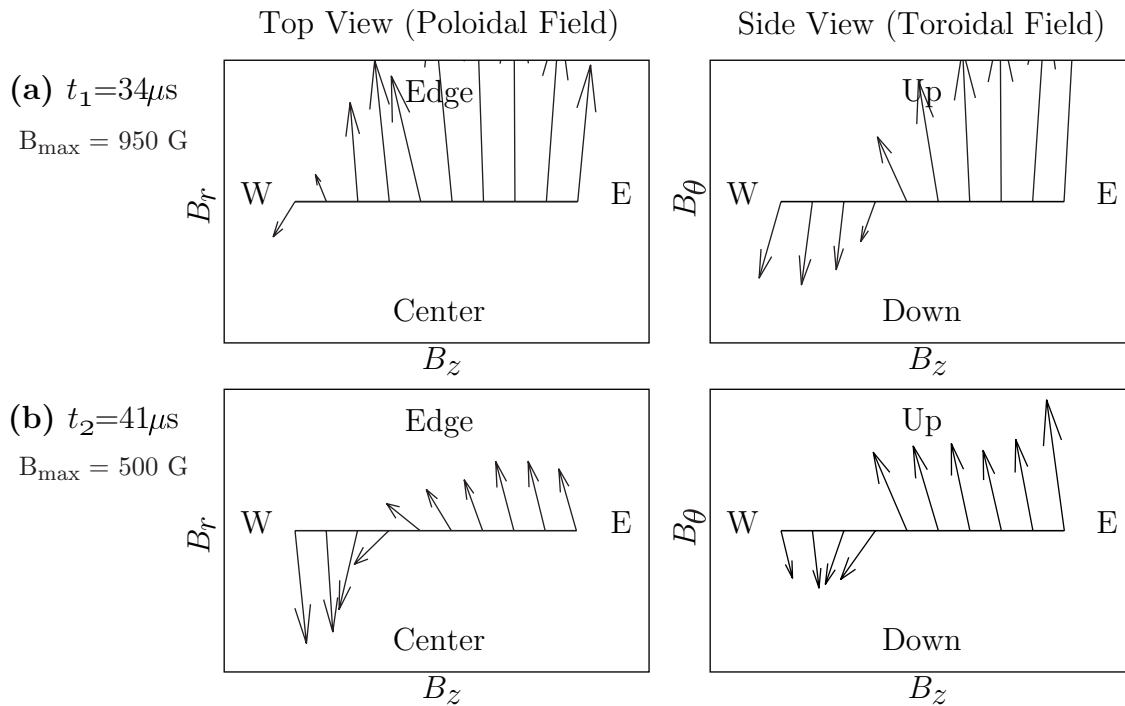


Figure 23: Poloidal and toroidal projections of the magnetic field in the reconnection region at time (a) t_1 before annihilation (b) t_2 after annihilation $7 \mu\text{s}$ later. Probe separation is 1 cm. (Run #13(98/1/26))

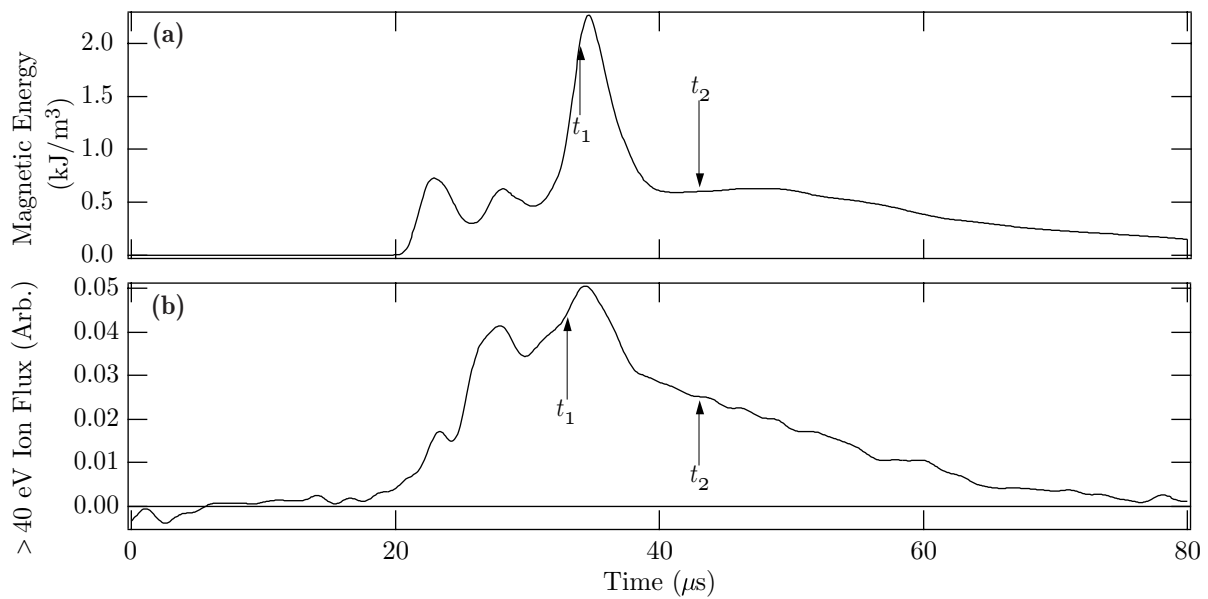


Figure 24: Time history of the run shown in figure 23. Plotted are the (a) local magnetic energy density and (b) energetic ion flux. (Run #13(98/1/26))

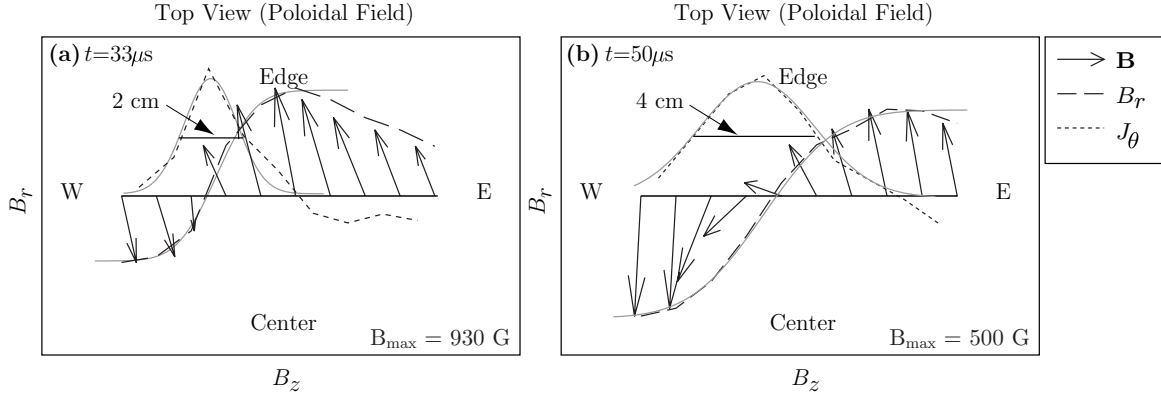


Figure 25: Detail of reconnection layer in the poloidal (r - z) projection at about t_1 in (a) and later in equilibrium in (b). Probe separation is 1 cm. (Run #14(98/1/26))

fact that the reconnection was being strongly driven by the large initial velocities of the two spheromaks. Later on in the same run (figure 25b), the spheromaks are no longer merging at high velocity and have reached equilibrium, allowing the layer to spread out a little to its equilibrium width. The width of the reconnection layer is measured to be ≈ 4 cm which is close to the collisionless reconnection prediction of $\delta_C = 2c/\omega_{pi} = 4.6$ cm. The Sweet-Parker prediction, on the other hand, is $\delta_{S-P} = 0.9$ cm which is much shorter than any thickness that we observe.

7.2 RGEA Results

We have performed scans of the retarding grid voltage on the RGEA to determine the average energy of the peak ion flux. In figure 26 we present escaping ion flux data as a function of energy for a single spheromak (legend: circles), two merging spheromaks with the detector out of the reconnection plane (legend: squares), and two merging spheromaks with the detector in the reconnection plane (legend: triangles). Each data point at a particular retarding voltage V_0 is constructed by averaging the peak flux values for 10 runs. The average energy \bar{E} for each spectrum is determined by fitting the data to the form $\Gamma = \Gamma_0 \exp(-V_0/\bar{E})$, as discussed in section 6.2. This analysis is only valid, however, for a thermalized velocity distribution. Note that the data fit a thermalized velocity distribution reasonably well.

Both the Sweet-Parker and the collisionless reconnection theories predict that the outflow velocity in the plane of reconnection should be Alfvénic. They disagree about whether the velocity distribution is unthermalized and entirely at the Alfvén speed, if it is generated already thermalized, or some combination of the two. The Sweet-Parker theory predicts that all the outflowing plasma should travel at the Alfvén speed since the convection of magnetic fields out of the reconnection layer is the acceleration mechanism. The RGEA spectrum for an entirely Alfvénic (unthermalized) flow would be a positive flat distribution as a function of increasing voltage for energies less than Alfvénic and zero for greater energies (a step function at the Alfvén speed). The collisionless reconnection theory, on the other hand, specifies electric fields as the acceleration mechanism for ions. If the incoming ions are thermalized, then the accelerated ions should also be thermalized with an additional offset representing

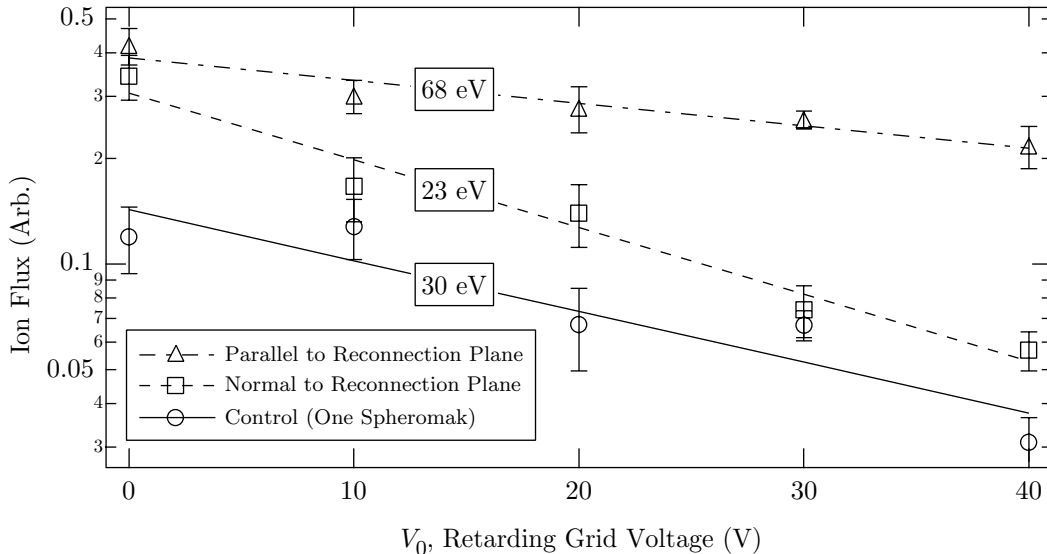


Figure 26: Energy spectrum of ions taken with the RGEA looking into the plane of reconnection, normal to the plane of reconnection and with only one spheromak as a control.

the bulk outflow velocity. The other way that the plasma can become thermalized is through collisions. Although the neutral pressure in the gap is low ($p_{base} = 10^{-8}$ torr), some plasma is present in the gap to thermalize the plasma beam during the experiment. If the plasma density is $n_e = 10^{14} \text{ cm}^{-3}$ in the gap, then the energetic ion mean free path is ≈ 25 cm. This will partially thermalize the beam in the 50 cm transit to the RGEA. Since the collisionless theory correctly predicts the magnetic profile width, we may assume that the outgoing ions are at least partially thermalized when they emerge from the reconnection region. That the ions are born partially thermalized and that they may be further thermalized in transit may be sufficient to explain the observed thermal distributions of the ion beams shown in figure 26.

Assuming that the ion beams are thermalized and that the analysis is justified, the data show interesting spatial variation of ion energy and flux. The ion flux from a single spheromak (26a) has a low average energy of $\bar{E} = 30$ eV, which is near the average temperature of the plasma $T_e = T_i \approx 20$ eV as measured by the triple probe (see appendix B). When two spheromaks are merged with the detector out of the plane of reconnection (26b), all of the accelerated ion flux is directed away from the RGEA and we do not expect to see any energetic ion flux. Indeed, the average energy \bar{E} is 23 eV, which is again close to the thermal energy. The total signal, however, doubles from $\Gamma_0 = 0.14$ to 0.31 when the second spheromak is added. This appears to be due to the fact that there is twice as much plasma in the chamber (with roughly constant temperature). When the RGEA is placed in the plane of reconnection, the accelerated ion flux is aimed directly at the RGEA and the in-plane reconnection flux (26c) is 25 percent larger than the out-of-plane flux and has a much higher average energy $\bar{E} = 68$ eV). The velocity of 68 eV protons corresponds to the Alfvén speed at $n_e \approx 10^{14} \text{ cm}^{-3}$ and $B \approx 500$ G. Note that the out-of-plane data run presented above suggests a small super-Alfvénic flow whereas the the out-of-plane spectrum

shows the background temperature of the plasma. The difference between these two measurements can be explained by the fact that the data run presented above was performed with the RGEA looking down a tube that restricted the viewable area of the experiment and blocked much of the background plasma from interfering with the low flux measurements. The spectrum was taken with the RGEA placed at the vacuum chamber wall so that it was accessible to particles coming from any point in the gap. Thus, the signal from the small flux of energetic particles was completely overwhelmed by the signal from the background plasma. Unfortunately, the spectrum was not taken above 40 eV. If it were, we would expect to see a second temperature emerge at a sufficiently low total flux level.

7.3 2D Data

Two dimensional maps of the magnetic field were recently created using the forest probe (described in section 6.1). The results presented in this section are preliminary, and the following analysis should be considered with this in mind. Additional measurements to verify these results are planned as part of the ongoing work in SSX.

Figure 27 shows projections of the magnetic field vectors in the r - z plane at two times during a typical run. After formation, the spheromaks enter the reconnection region at approximately the Alfvén speed, $10 \text{ cm}/\mu\text{s}$. The spheromaks initially create an X-point when they come in contact, as shown in figure 27a. The third column of the 2D data corresponds to the magnetic profiles obtained using the linear probes (compare figure 21a). The maximum magnetic field, $B_{max} = 1000 \text{ G}$, is similar to the maximum field in the linear probe measurements. The agreement between the linear probe data and 2D probe data builds confidence in both data sets.

About $2 \mu\text{s}$ after the formation of the X-point structure, a magnetic O-point develops. The O-point persists as the spheromaks reach equilibrium, as shown in (27b). The layer is dynamic and the O-point moves toward the center of the array by time t_2 . In light of these observations, the linear probe profile in figure 21b could be reinterpreted as the result of rapid O-point formation. The linear profile is similar to the third column of the 2D data (immediately to the left of the O-point in figure 27b). If we accept this analysis, the burst of energetic particles could be due to the fact that the X-point lasts for a short time in these conditions.

Initially, the West spheromak is much stronger than the East spheromak and distends most of the way across the gap (27a). The magnetic structures are seen to move freely across the gap, indicating that the gap does not define the width of the reconnection layer. This is an important observation because it validates our previous measurements on the width of the layer. The linear probe runs were carefully chosen to have the annihilation event take place without any convection of the magnetic structures out of the gap.

If the O-point appears, it will almost always appear immediately after the spheromaks initially merge, when one or both of the spheromaks are in the process of bouncing off the back wall. This phenomenon is similar to experiments at MRX by Yamada et al. (1997) that show that O-points are generated as spheromaks are pulled apart. They observe that O-points were created during co-helicity reconnection (using two right- or two left-handed spheromaks). They postulate that the existence of the O-point slows the rate of co-helicity reconnection. Unlike MRX, we observe O-points generated during counter-helicity merging.

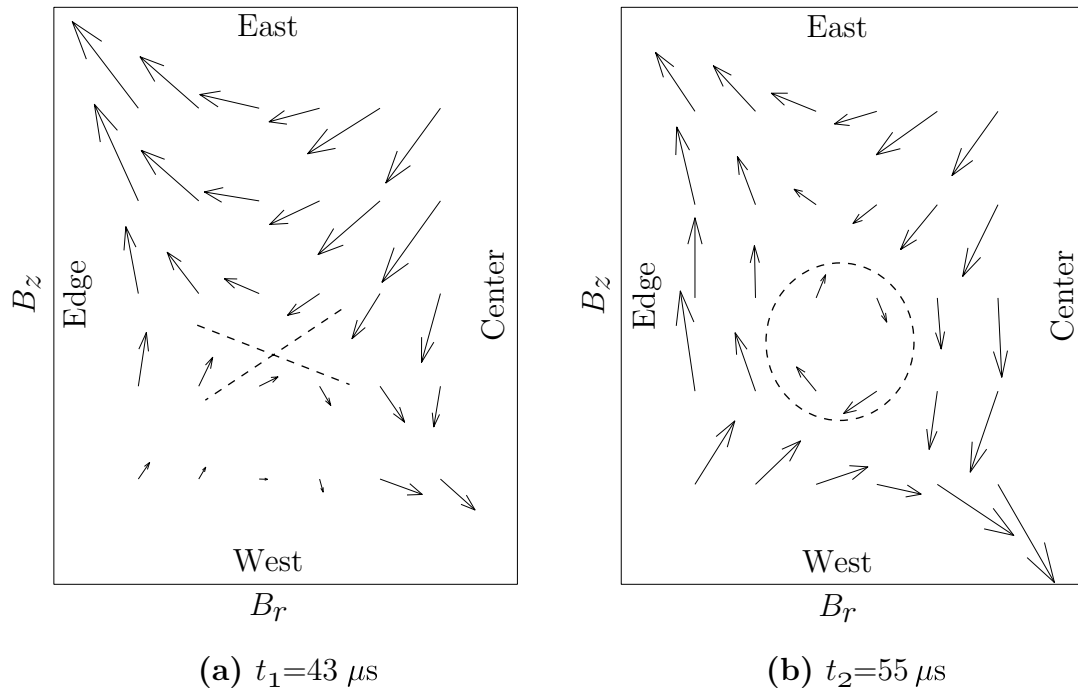


Figure 27: 2D map of the magnetic field showing evolution of a magnetic O-point. Magnetic field vectors, projected onto the r - z plane, are shown with an X-point at time t_1 in (a) and with an O-point at time t_2 in (b), $13 \mu s$ later. $B_{max} = 1000$ G. Probe separation is $\Delta r = .6$ cm and $\Delta z = .75$ cm. (Run #05(98/4/20))

The author is not aware of any previous experiments that report O-points in counter-helicity reconnection. Since SSX does not have control over the position of the spheromaks, one is not able to directly verify that the reconnection rate slows down when O-points appear. However, the reconnection rate can be inferred from the particle flux. Upon reanalysis of the linear probe data, the decrease in fields was speculated to be due to O-point formation. If one believes this reanalysis is correct, then the X-point should produce a large flux of high energy particles, whereas the subsequent O-point produces much less flux. Thus, O-points have a slower reconnection rate than X-points.

Matthaeus et al. (1984) show that these O-points can arise as a result of turbulence. O-points were very common in the 2D data runs, and they tended to be more common in higher magnetic energy runs. Turbulence becomes increasingly significant as the magnetic Reynolds number increases. Since increasing the magnetic energy increases the Reynolds number, then we expect the turbulent formation of O-points to be more frequent. Although this is a compelling trend in support of the turbulence explanation, the sample size in support of this trend is very small. A systematic investigation is necessary to verify this observation.

The magnetic structures varied considerably among runs using the same parameters. Sometimes O-points appeared and other times they did not. This observation emphasizes the importance of sampling all the probes simultaneously and not averaging data between different runs. Except for the RGEA spectrum, none of the data presented here was composed of averaged runs.

Note that the forest probe was built only recently, precluding a more thorough presentation of the results. Measurements of the out-of-plane field structure and the particle flux were not accomplished, but are planned for future experiments.

8 Concluding Remarks

This thesis details how I have used analytical models and experimental measurements to understand the magnetic reconnection generated by merging two spheromaks. The spheromaks initially merge at high velocity and exhibit a transient, thin reconnection layer indicative of driven reconnection. The layer widens to the collisionless reconnection prediction $\delta_C = 2c/\omega_{pi}$ as the system reaches a steady state. Correlated with the annihilation of magnetic flux are peaks in the energetic ion flow in the plane of reconnection. These observations for a single run are supported statistically by the energetic particle spectra. The spectra verify that the ion flux out of the reconnection plane is directional. Parallel to the reconnection plane, the flux is large and Alfvénic whereas normal to the reconnection plane, the flux is small and is at the background temperature. We also have data that suggest that a small flux of super-Alfvénic particles is emerging normal to the plane of reconnection as predicted by the simulations of turbulent reconnection. These data are further supported by the observation of O-points in the reconnection layer. The experiments simultaneously support the collisionless reconnection theory and the turbulent reconnection theory. We were not able to measure super-Alfvénic electron jets or out-of-plane magnetic fields at the c/ω_{pe} scale as predicted by the collisionless reconnection model. We do not have the spatial resolution or sensitivity to measure such effects ($c/\omega_{pe} \approx 0.5$ mm in our experiment).

Magnetic reconnection in solar and magnetotail physics may benefit from these results. In the past, purely resistive MHD models have been employed to model solar flares and the earth's magnetotail. In a very low density plasma, such as the solar wind and the magnetotail, the collisionless reconnection theory may be essential to model the dynamics correctly. Solar flares may have a sufficiently high density to preclude the use of collisionless reconnection theory.

Reconnection studies on SSX will continue with a 3D probe array and over 600 channels of data acquisition. Accurate temperature measurements using a vacuum monochromator will provide more accurate values for many experimentally determined plasma quantities. These upcoming experiments will provide valuable data concerning the 3D magnetic reconnection structure. The new measurements will provide an understanding of characteristics that were difficult to interpret because of the small cross section of data provided by the linear and 2D probes.

Appendix A: Derivation of the Generalized Ohm's Law

A simplified equation of motion for the electrons in a plasma includes terms for electromagnetic interactions, electron pressure and collisional viscosity. The electromagnetic interactions are governed by the Lorentz force (1). The electron pressure force (3) acts against electrons moving up pressure gradients. The resistive force (5) is due to collisions with ions and is proportional to the velocity of the electrons. And finally, the viscous force (4) governs momentum transfer between electrons (and, as such, can be grouped with the pressure force). The equation of motion for an electron can therefore be written as it appears in equation (8):

$$ma = \sum F \quad (64)$$

$$m_e n \frac{d\mathbf{v}_e}{dt} = m_e n \left(\frac{\partial \mathbf{v}_e}{\partial t} + (\mathbf{v}_e \cdot \nabla) \mathbf{v}_e \right) = \underbrace{-en(\mathbf{E} + \mathbf{v}_e \times \mathbf{B})}_{\text{Lorentz Force}} - \underbrace{\nabla p_e}_{\text{Pressure}} - \underbrace{\nabla \cdot \tilde{\pi}_e}_{\text{Viscosity}} + \underbrace{R(\mathbf{v}_e)}_{\text{Resistivity}} \quad (65)$$

where p_e is the electron pressure, $\nabla \cdot \tilde{\pi}_e$ is the electron viscosity and R is the resistive momentum transfer term due to collisions with ions. The momentum transfer term scales like the collision frequency and assuming isotropic collisionality, the resistivity can be written as linear function of the current:

$$R = m_e n \langle \nu_{coll.} \rangle (\mathbf{v}_i - \mathbf{v}_e) = \eta e^2 n^2 (\mathbf{v}_i - \mathbf{v}_e) = \eta en \mathbf{J} \quad (66)$$

The electron velocity can be expressed in terms of the directly measurable quantities, ion velocity (\approx bulk plasma flow) and current:

$$\mathbf{J} = -en(\mathbf{v}_e - \mathbf{v}_i) \Rightarrow \mathbf{v}_e = \mathbf{v}_i - \frac{\mathbf{J}}{en} \quad (67)$$

Neglecting the nonlinear convective derivatives, $(\mathbf{v}_e \cdot \nabla) \mathbf{v}_e$, and replacing the electron velocity with the latter equation yields:

$$m_e n \frac{\partial}{\partial t} \left(\mathbf{v}_i - \frac{\mathbf{J}}{en} \right) = -en \mathbf{E} + \left(\mathbf{v}_i - \frac{\mathbf{J}}{en} \right) \times \mathbf{B} - \nabla p_e - \nabla \cdot \tilde{\pi} + R \quad (68)$$

In the quasi-static approximation, the magnetofluid moves much more slowly than the electrons, allowing us to eliminate $|\partial \mathbf{v}_i / \partial t| (\ll |\partial \mathbf{v}_e / \partial t|)$. In the MHD regime, where the electrons are frozen into the flux, the flow velocity of the ions represents the flow of the entire magnetofluid and so $\mathbf{v}_i \approx \mathbf{v}$. This approximation justifies how we have neglected the ion equation of motion and focused almost entirely on the electron dynamics. With these approximations, the familiar form of Ohm's law appears:

$$\mathbf{E} + \mathbf{v} \times \mathbf{B} = \eta \mathbf{J} + \frac{1}{en} \mathbf{J} \times \mathbf{B} - \frac{1}{en} \nabla p_e - \frac{1}{en} \nabla \cdot \tilde{\pi}_e + \frac{m_e}{e^2 n} \frac{\partial \mathbf{J}}{\partial t} \quad (69)$$

This form of Ohm's law is a general description of the plasma motion in the quasi-static MHD regime, excluding inhomogeneous density and pressure corrections. The viscosity term can

be neglected for large collision frequency ν_{ii} according to the Navier-Stokes theory (Krall and Trivelpiece, 1973):

$$\tilde{\pi} \text{ can be neglected if } R \equiv \frac{Lv_0m\nu_{ii}}{kT} \gg 1 \quad (70)$$

R is called the Reynolds number (not to be confused with the magnetic Reynolds number) and L and v_o are characteristic length and velocity of the plasma. Even for collisionless plasmas, this convenient approximation holds. According to Krall and Trivelpiece, “It is a fortunate fact that the plasma equations with $[\nabla \cdot \tilde{\pi} + \nabla p] = \nabla p$ agree with a wide range of experiments, despite a lack of a clear basis for that approximation.” [(Krall and Trivelpiece, 1973), p. 94]. Thus, neglecting the viscosity term yields:

$$\mathbf{E} + \mathbf{v} \times \mathbf{B} = \eta \mathbf{J} + \frac{1}{en} \mathbf{J} \times \mathbf{B} - \frac{1}{en} \nabla p_e + \frac{m_e}{e^2 n} \frac{\partial \mathbf{J}}{\partial t} \quad (71)$$

This form of Ohm’s law that serves as the starting point for the theories above. In the case of high density, Ohm’s law reduces to the purely resistive case:

$$\mathbf{E} + \mathbf{v} \times \mathbf{B} = \eta \mathbf{J} \quad (72)$$

The high density case is not always a good approximation and can sometimes lead to incomplete descriptions of the plasma dynamics. The purely resistive Ohm’s law is used in the Sweet-Parker model whereas the collisionless reconnection model, as its name implies, includes the other terms.

Appendix B: Triple Probe Measurements

A triple probe has three tips of wire which can be used to measure the temperature and density of a plasma simultaneously. Before delving into the details and complexity of the triple probe, let us first discuss the plasma interaction with a single tip of wire, called a Langmuir probe.

The Langmuir probe is placed in the plasma and biased at various voltages to measure the temperature and density of the plasma. The voltage creates an electric field at the tip of the probe which attracts electrons or ions depending on the sign of the bias voltage. Current is measured in the circuit completed by the plasma whose source connects to a common ground with the voltage supply. This current is called the probe current I and is simply the sum of the electron and ion currents:

$$I = -(I_i - I_e) \quad (73)$$

If the electrons are thermalized, an expression for the electron current can be obtained using the Maxwell velocity distribution by selecting only those electrons that can overcome the potential barrier to the probe tip. Namely, those electrons that have energy greater than $V_s - V$ where V is the bias voltage and V_s is the plasma (space) potential. The electron current is thus given by:

$$I_e = Aen_e \int_{\sqrt{2e(V_s-V)/m_e}}^{\infty} v \exp\left(-\frac{m_e v^2}{2T_e}\right) dv \quad (74)$$

$$= Aen_e \sqrt{\frac{T_e}{2\pi m_e}} \exp\left(-\frac{e(V_s - V)}{T_e}\right) \quad (75)$$

where T_e is the temperature of the electrons in eV. The number of electrons reaches a plateau as the bias voltage is turned up. That maximum current is called the saturation current and is given by the maximum of equation (75):

$$I_- = Aen_e \sqrt{\frac{T_e}{2\pi m_e}} \quad (76)$$

The electron current saturates when almost all electrons in the vicinity of the probe are collected and no more can be collected without ionizing more ions.

A similar treatment of the ion current is possible, but because the mass of the ion is many magnitudes greater than that of the electron, changes due to the ion velocity distribution do not affect the total probe current significantly. Instead, the ion gas is considered to be very cold and virtually collisionless. The ion current is determined using the concept of the Debye sheath which is the region through which most of the probe potential drops off and the attractive gradient is very high. Because of the strong potential gradient below the Debye sheath at large negative biases, ions are almost exclusively collected on the probe. Following these considerations Bohm (Bohm et al., 1949) showed that a convenient approximation to the ion current can be written as:

$$I_i = I_+ = Aen_i \sqrt{\frac{2T_i}{m_i}} \quad (77)$$

This approximation is usually sufficient because the heavy ions are usually overwhelmed by the lightweight and faster electron current.

Now that we have expressions for the electron and ion currents, equation (73) now expresses the probe the probe current in terms of electron temperature, density and other known quantities. A convenient form to calculate the electron temperature is derived by taking the natural log of the electron current equation (75) and differentiating both sides with respect to the bias voltage. Since the ion current and the electron density are constant, the result is simply:

$$\frac{d}{dV} \ln(I) = \frac{e}{T_e} \quad (78)$$

Plotting $\ln I$ in the region of constant slope allows easy determination of the temperature of the electrons. Having calculated the temperature of the plasma and having measured the electron saturation current, equation (76) determines the density of the plasma.

We are now prepared to discuss the triple probe. The Langmuir probe works very well but requires a large set of data to be taken sequentially for various bias voltages. The triple probe takes two simultaneous measurements to solve for both temperature and density at the same time.

The analysis presented here comes from Ji et al. (1991). Consider three Langmuir probes labeled P_1 , P_2 and P_3 inserted into a plasma. They are connected by the circuit shown in figure 28a. A constant voltage V_{d3} is applied between P_1 and P_3 using a charged capacitor. The voltage V_{d2} between P_1 and the floating P_2 (at the floating voltage V_f) is measured using an isolation transformer. The potentials are displayed graphically in figure 28b. With an eye on this figure, we can write expressions for the directly measured voltages:

$$V_{d2} = V_2 - V_1 \quad (79)$$

$$V_{d3} = V_3 - V_1 \quad (80)$$

The currents flowing into each of these probes can be written using the expression (75) for a single Langmuir probe with various voltages:

$$P_1 : \quad -I_1 = -I_- \exp\left(-\frac{V_1}{T_e}\right) + I_+ \quad (81)$$

$$P_2 : \quad 0 = -I_- \exp\left(-\frac{V_2}{T_e}\right) + I_+ \quad (82)$$

$$P_3 : \quad I_1 = -I_- \exp\left(-\frac{V_3}{T_e}\right) + I_+ \quad (83)$$

The previous five equations can be combined to produce the following two transcendental equations:

$$\frac{1}{2} = \frac{1 - \exp(-V_{d2}/T_e)}{1 - \exp(-V_{d3}/T_e)} \quad (84)$$

$$I_+ = I_1 \frac{\exp(-V_{d2}/T_e)}{1 - \exp(-V_{d2}/T_e)} \quad (85)$$

The numerical solutions to these equations are plotted in figure 29.

Note that for low applied voltages V_{d3} , the temperature increases very rapidly with changes in measured voltage V_{d2} . This is because high energy electrons will not be significantly attracted to a probe that has a bias voltage that is low compared to the electron's energy. A measurement of temperature under such circumstances is difficult because the signal is very small. The plots in figure 29a are linear for $T_e < V_{d3}/2$ and divergent elsewhere. To get an accurate measurement of temperature T_e , it is necessary to have the applied voltage of $V_{d3} \gg 2T_e$. Subjecting the transcendental equations (84) and (85) to this approximation gives an easy form:

$$\frac{T_e}{V_{d2}} \simeq \frac{1}{\ln 2} \quad (86)$$

Which is the slope of the linear part of all the curves in figure 29a.

A triple probe was used to measure the temperature and density of spheromaks created using the coaxial plasma guns in SSX. The results are shown in figure 30 for typical gun parameters ($V_{gun} = 5$ kV, $B_{stuff} = 1.5$ mWb). The triple probe tip was placed halfway between the toroidal axis and the edge of the spheromak for this run. The temperature climbs sharply when the spheromak enters the flux conserver and plateaus for the lifetime of the spheromak, after which confinement is lost and the temperature and density drop off to zero. On the plateau, we can safely claim $T_e \approx 20$ eV and $n_e \approx 10^{14}$ cm⁻³. Perhaps the most interesting feature of this measurement is that the temperature and density are nearly constant throughout the lifetime of the spheromak. This shows that the spheromak is a stable source of magnetofluid for reconnection experiments and we do not need to be concerned with how the temperature and density of the plasma change with time when analyzing reconnection data.

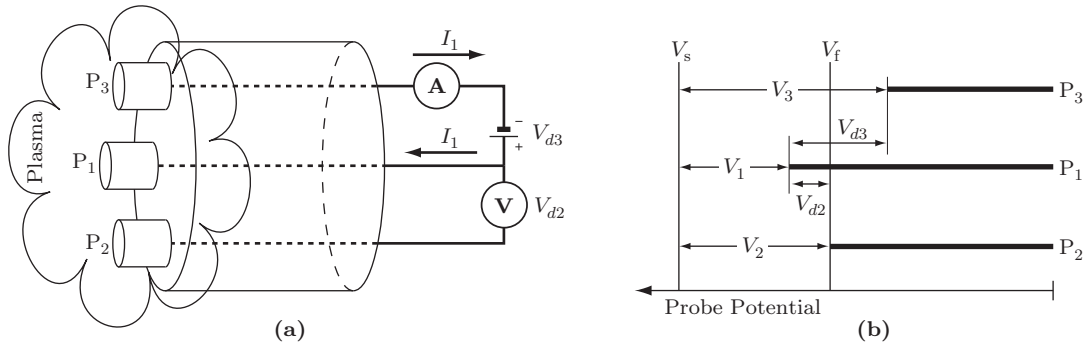


Figure 28: Schematic of the triple-probe design and circuit. Adapted from figures in Ji et al. (1991).

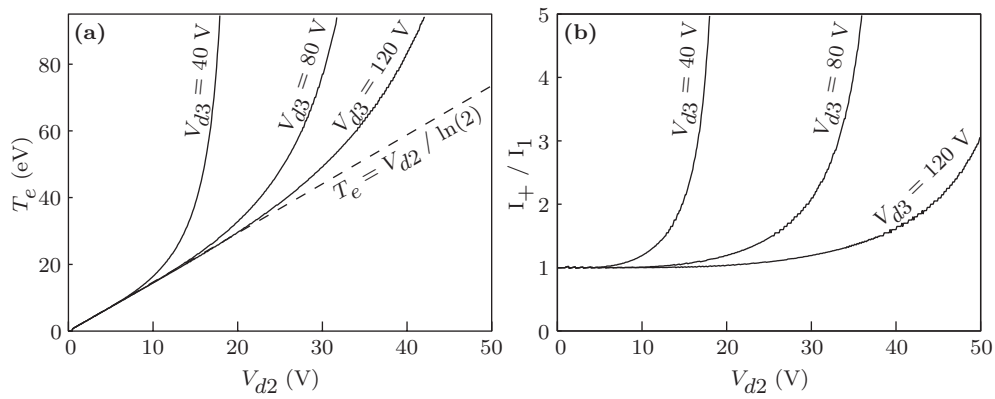


Figure 29: Solutions to the transcendental equations (85) and (84), showing the temperature (a) and ion saturation current (b) as a function of the measured voltage V_{d2} for three applied voltages V_{d3}. Adapted from figures in Ji et al. (1991).

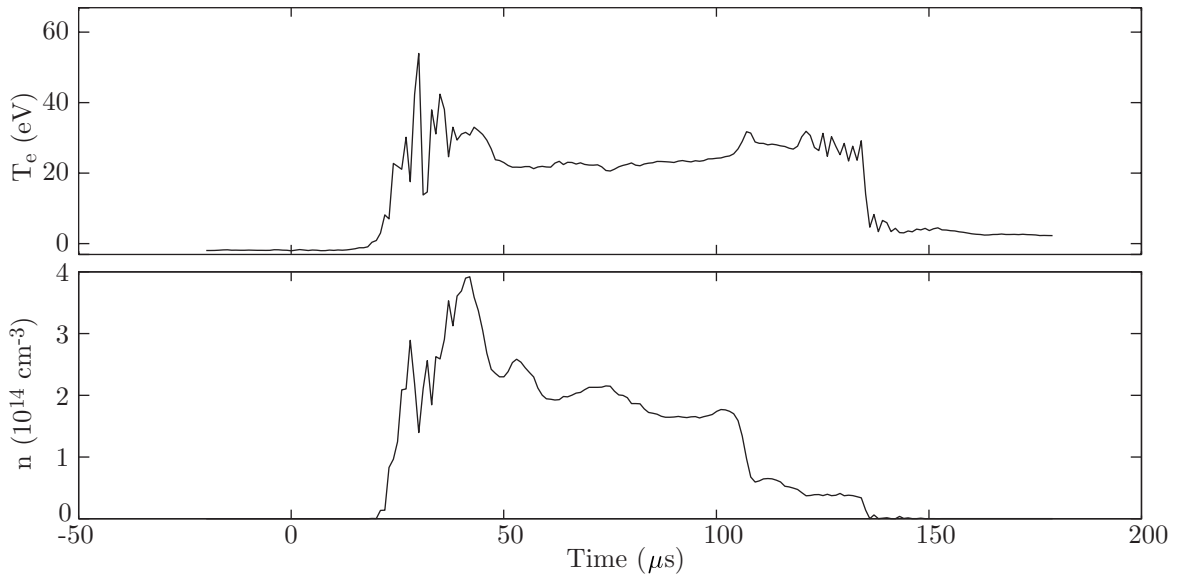


Figure 30: Triple probe results showing time resolved temperature and density.

Appendix C: The Spheromak Formation Threshold

The coaxial plasma gun forms spheromaks by accelerating them through a strong magnetic field. If the magnetic tension of the stuffing field exceeds the magnetic pressure of the $\mathbf{J} \times \mathbf{B}$ force, then a spheromak is formed. However, if the gun current is insufficient and the stuffing field too strong, then the plasma will bounce off the stuffing field and remain “stuffed” in the gun. For a given stuffing field, there is a *threshold* gun current beyond which spheromaks are formed and before which spheromaks are stuffed.

A simple formation theory can be constructed as follows. This theory is presented in Geddes, Kornack, Brown (1998). Assume a thin radial current sheet through an annulus of plasma that is free to move axially (see figure 31). The stuffing field is completely radial at the opening of the gun. Force balance on the current sheet requires that the magnetic tension of the stuffing flux equals the net $\mathbf{J} \times \mathbf{B}$ force. Since the gun current produces an azimuthal field $B_\theta = \mu_0 I_{gun}/2\pi r$, we can write the magnetic pressure on the back of the sheet as:

$$P_B = \frac{B_\theta^2}{2\mu_0} = \frac{\mu_0 I_{gun}^2}{8\pi^2 r^2} \quad (87)$$

If we integrate this pressure over the annular face of the current sheet, we find for the net $\mathbf{J} \times \mathbf{B}$ force:

$$F = \int_{r_{inner}}^{r_{gun}} P_B r dr d\theta = \frac{\mu_0 I_{gun}^2}{4\pi} \ln\left(\frac{r_{gun}}{r_{inner}}\right) \quad (88)$$

Now if the stuffing flux is distend an amount δz by this force due to the magnetic pressure P_B , then the work done by this force equals the increase in magnetic energy. That magnetic energy goes into distending the stuffing field:

$$F\delta z = \Delta W_{mag} \gtrless \frac{B_{stuff}^2}{2\mu_0} (\pi r_{inner}^2) \delta z \quad (89)$$

On the threshold of formation, the work done by the gun field is balanced by work it takes to distend the stuffing field, so the \gtrless becomes an $=$. Now, the stuffing flux is $\Phi_{stuff} = B_{stuff} \pi r_{inner}^2$ since it passes through the inner electrode before becoming radial at the opening of the gun. Rewriting and labeling a new quantity λ_{th} , we find:

$$\lambda_{th} \equiv \frac{\mu_0 I_{gun}}{\Phi_{gun}} = \frac{1}{r_{inner}} \sqrt{\frac{2}{\ln(r_{gun}/r_{inner})}} \quad (90)$$

for the threshold. According to this theory, plotting the threshold point as a function of gun current $\mu_0 I_{gun}$ and stuffing flux Φ_{gun} , the threshold would be a line of slope λ_{th} . For increasing gun current and decreasing stuffing field on the threshold, spheromaks are formed. Otherwise, the stuffing field is too strong to overcome and the plasma remains stuffed in the gun.

This theory has been experimentally verified and the results are shown in figure 32. For our parameters ($r_{gun} = 8.3$ cm and $r_{inner} = 3.1$ cm), the formation threshold is

$\lambda_{th} = 46 \text{ m}^{-1}$. Scans of poloidal (B_z) magnetic data were taken at the edge of both large and small flux conservers. Data were taken from $\Phi_{stuff} = 0$ to 2.0 mWb at 0.25 mWb intervals and from $I_{gun} = 0$ to 100 kA at 10 kA intervals (a 9×11 matrix). Averages of several runs were taken each operating point.

There is a formation threshold in both flux conservers at $\lambda_{th} = \mu_0 I_{gun} / \Phi_{stuff} \cong 48 \text{ m}^{-1}$ which is close to the value of $\lambda_{th} = 46 \text{ m}^{-1}$ predicted by theory. This threshold does not scale with the dimensions of the flux conserver attached to the gun and depends only on gun dimensions which remain constant through the experiments.

A few other features are worth noting. When the stuffing flux is very low ($\Phi_{stuff} \rightarrow 0$), the spheromak fields vanish even for large gun currents I_{gun} . We took an extra set of data at $\Phi_{stuff} = 0.1$ mWb to verify this observation. The gun will not operate at zero stuffing flux because as $\Phi_{stuff} \rightarrow 0$ the injected helicity vanishes and a finite helicity object like a spheromak cannot be formed (Barnes et al., 1986). In the large flux conserver we find that the spheromak fields vanish at small but finite I_{gun} and Φ_{stuff} (even with $\lambda > \lambda_{th}$). This is a reproducible result for which we have no explanation.

These data indicate the optimal regimes for operating the coaxial plasma guns. We use this information to reliably produce spheromaks for use in the reconnection experiments.

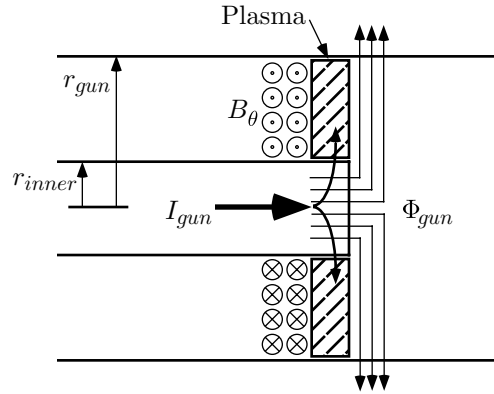


Figure 31: Simple diagram for spheromak formation.

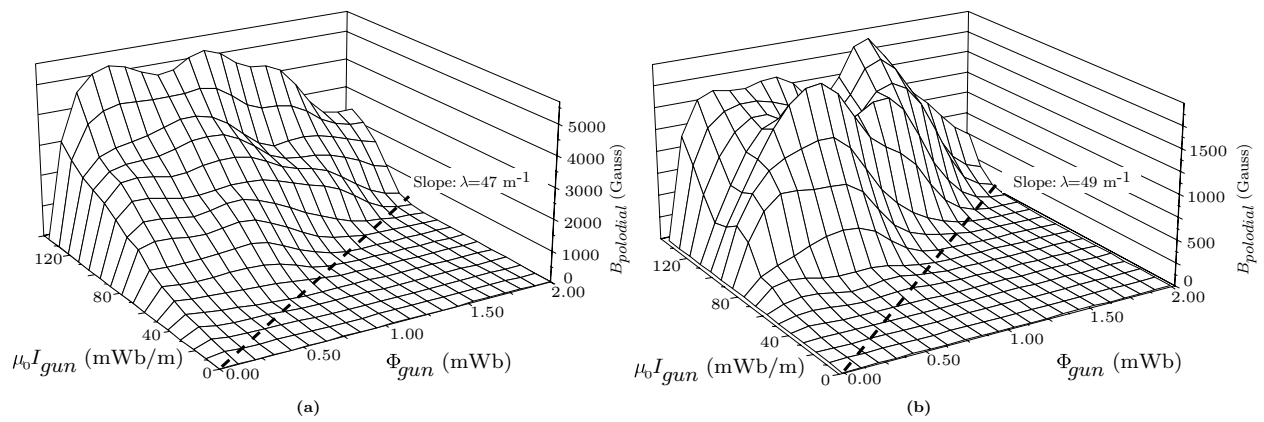


Figure 32: Plots of spheromak fields $B_{poloidal}$ for spheromaks formed into small (a) and large (b) flux conservers as a function of gun current I_{gun} and stuffing flux Φ_{stuff} .

Appendix D: Fast Pulse Gas Valve Design

The gas valves used in SSX are the result of three years of research and development by the author. The original design goal was to produce a 300 μs pulse of hydrogen as obtained by Thomas et al. (1993). The short pulse of gas would deliver only as much gas as is necessary to form a spheromak in the coaxial plasma guns. With a longer pulse, the spheromak could ionize the head of the gas pulse but would then encounter continued flow of neutral hydrogen gas which would cool the plasma and ruin confinement. This appendix contains a description of the final design and summarizes the lessons learned from previous generations of valve designs.

The valve design is shown in figure 33; a picture of the final product is shown in figure 18. A circular aluminum poppet rests on a small O-ring that seals the high vacuum from the pressurized hydrogen. Hydrogen gas is introduced through the connectors on the top and is pressurized to a 4-6 atm. The higher pressure tends to make the valve close more quickly and offer a higher density burst of gas. An additional retarding force is supplied by a strong (72 lb/in) spring which pushes the poppet closed against the O-ring. A flat electromagnetic coil lies immediately beneath the poppet, with a thin (1/32 in) stainless steel wall in between to keep the hydrogen gas inside. The casing is made out of stock stainless steel ConFlat flange endcaps and adapters to make machining and assembly easier.

The valve is opened by sending a short ($\leq 100 \mu\text{s}$) pulse of 1-2 kA which through the flat coil that rests beneath the poppet. For a good conductor like aluminum, flux is excluded over a characteristic soak time $\tau_{soak,Al}=340 \mu\text{s}$ for a 1/16 in thick sheet of aluminum. The magnetic pressure between the coil and the aluminum poppet forces the poppet up and the valve open.

To make a fast gas valve, the circuit completed by the coil and the power supply must be capable of fast pulses of high current. For a capacitive power supply connected to an inductive load, we want the quarter-cycle rise time to be less than 100 μs

$$\tau_{rise} = \frac{\pi}{2} \sqrt{LC} \leq 100 \mu\text{s} \quad (91)$$

where L is the inductance of the coil in the gas valve and C is the capacitance of the power supply. The energy required to open the valve was experimentally determined to be approximately 10 J. The energy stored in a capacitor is

$$10 \text{ J} = \frac{1}{2} CV^2 \quad (92)$$

Thus, for any decrease in capacitance, the voltage must increase quadratically to maintain sufficient energy to open the valve. To keep voltages low, we chose to charge an 88 μF capacitor to 500 V. To keep the the circuit as fast as possible, we chose the coil to be 4 μH , putting the rise time at 30 μs . The circuit was switched using an SCR (Silicon Controlled Rectifier) connected to a fiber optic trigger circuit.

At such low inductances, the inductance of the entire circuit becomes significant. The total energy stored in the power supply is distributed linearly with inductive elements in the circuit. If the circuit has as much as 0.5 μH due to loops of wires connecting various components, then as much as 12 percent of the power will not be stored in the coil. Much of the circuitry is therefore connected with coaxial cable which has a very low inductance.

Note the annular region cut out of the bottom ConFlat flange that immediately surrounds the O-ring. This annulus is designed to contain a pocket of hydrogen gas that can flow unobstructed past the O-ring and down the tube when the valve opens. This ensures that sufficient gas is available to be injected in the short amount of time that the valve is open. For SSX, the valve delivers a volume $\approx 1 \text{ cm}^3 \text{ H}_2$ at 1 atm per pulse which is introduced into the gun in annular region between the electrodes. This volume corresponds to a maximum particle inventory of $N \leq 10^{18}$ ions or electrons per spheromak. The charging voltage on the capacitive power supply can be varied slightly to calibrate each valve's total output. The valve can be operated in a wide range of output volumes.

The gas valve was tested in vacuum with a fast ionization gauge (FIG) to measure transient pressure. A curly loop of tungsten wire carries 1-5 A and ionizes any nearby particles of gas. Two bare wire tips are held at a voltage difference of more than 40 V. The newly ionized electrons and ions separate and flow to the tips where they are collected. The current is recorded and is proportional to the pressure of the gas at the probe tip. Figure 34 shows a typical pulse of gas for the circuit setup described above. The gas valve and FIG were installed in the coaxial plasma gun so that they were on opposite sides of the inner electrode. The data show a sharp rise for 300 μs followed by a 100 μs plateau. The asymptotic decay is probably due to the relatively slow pumping rate of the cryopump on these timescales. Since the FIG does not look directly at the output of the gas valve, the timing may be smoothed and drawn out a little due to collisions in getting around the electrode. The peak in pressure occurs at around 750 μs after the trigger; this is the time when the high voltage is fired to ionize the gas and form a spheromak. The transit speed for neutral hydrogen is a slow 1 m/ms, so the gas does not leak out of the gun appreciably before the ionization.

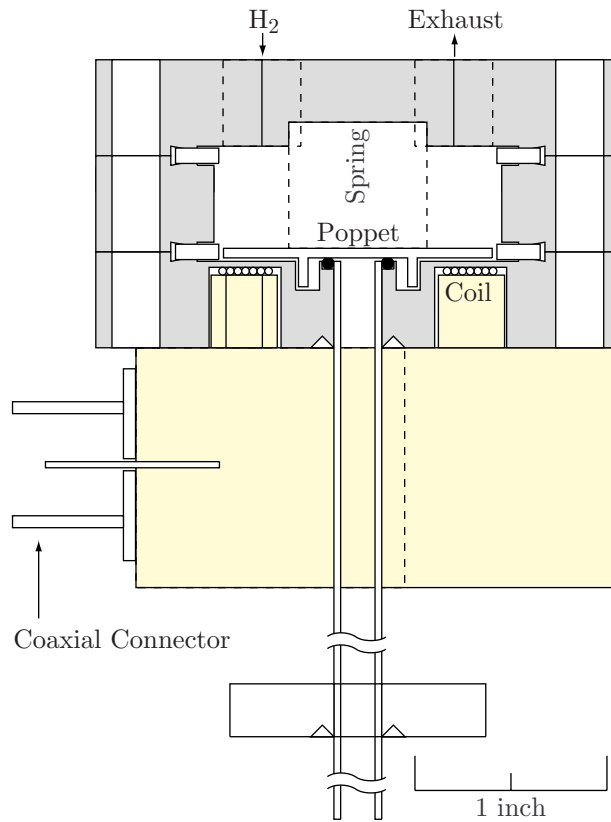


Figure 33: Cutaway view showing the essential components of the gas valve design. Note the annular space adjacent to the O-ring which is designed to contain a pocket of gas. A picture of the final product is shown in figure 18.

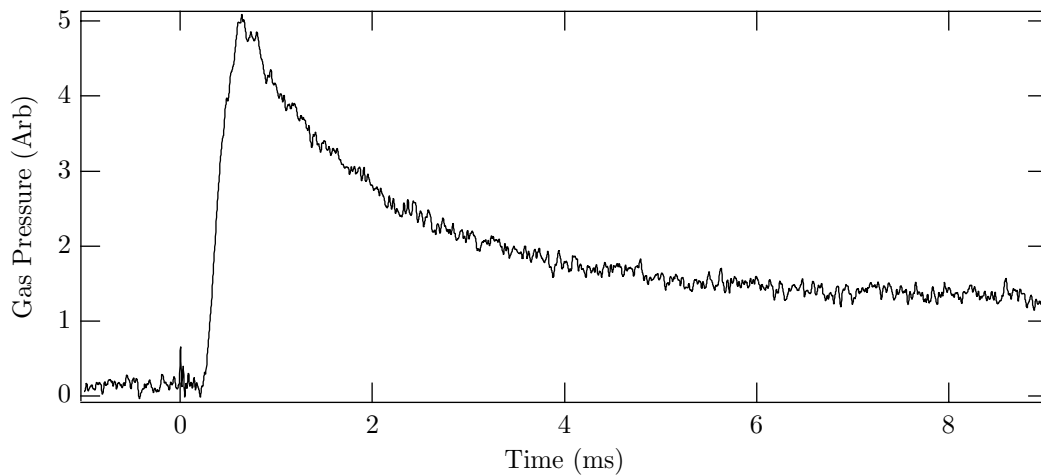


Figure 34: Time resolved gas pressure near the gas valve output. Measured with a fast ionization gauge. The zero level corresponds to 10^{-8} torr.

Appendix E: Acknowledgements

The author deeply appreciates all that his advisor, Michael Brown, and fellow researchers Cameron Geddes and Peter Sollins have done for their help, ideas, and cooperation in this project. Tremendous thanks to Steve Palmer for construction of the experimental apparatus and probes and to David Radcliff for construction of the electronics and cabling. The contributions and support from these people have been invaluable throughout this project. Financial support has been provided by the Department of Energy, Research Corporation, the Petroleum Research Fund, and the NASA Delaware Space Grant Consortium.

References

- Ambrosiano, J. J., Matthaeus, W. H., Goldstein, M. L., and Plante, D. (1988). Test particle acceleration in turbulent reconnecting magnetic fields. *Journal of Geophysical Research*, 93:14383.
- Aschwanden, M. J., Hudson, H., Kosugi, T., and Schwartz, R. A. (1996). Electron time of flight measurements during the masuda flare. *Astrophys. J.*, 464:985.
- Aschwanden, M. J., Schwartz, R. A., and Alt, D. M. (1995). Electron time of flight differences in solar flares. *Astrophys. J.*, 447:923.
- Barnes, C. W., Fernández, J. C., Henins, I., Hoida, H. W., Jarboe, T. R., Knox, S. O., Marklin, G. J., and McKenna, K. F. (1986). Experimental determination of the conservation of magnetic helicity from the balance between source and spheromak. *Physics of Fluids*, 29(10):3415.
- Birn, J., Forbes, T. G., Hones, E. W., and Bame, S. J. (1981). On the velocity distribution of ion jets during substorm recovery. *Journal of Geophysical Research*, 86:9001.
- Biskamp, D. (1997). Magnetic reconnection in plasmas. *Astrophysics and Space Science*, 242:165.
- Biskamp, D., Schwartz, E., and Drake, J. F. (1995). Ion controlled collisionless magnetic reconnection. *Physical Review Letters*, 75:3850.
- Biskamp, D., Schwartz, E., and Drake, J. F. (1997). Two-fluid theory of collisionless magnetic reconnection. *Physics of Plasmas*, 4(4):1002.
- Bohm, D., Burshop, E. H. S., and Massey, H. S. W. (1949). *The Characteristics of Electrical Discharges in Magnetic Fields*. McGraw-Hill, New York.
- Chen, F. F. (1983). *Introduction to Plasma Physics and Controlled Fusion*. Plenum Press, New York.
- Geddes, C. G. R. (1997). Equilibrium studies on ssx. Undergraduate thesis, Swarthmore College.
- Geddes, C. G. R., Kornack, T. W., and Brown, M. R. (1998). Scaling studies of spheromak formation and equilibrium. *Physics of Plasmas*, 5:1027.
- Gekelman, W., Stenzel, R. L., and Wild, N. (1982). Magnetic field line reconnection experiments: 3. ion acceleration, flows, and anomalous scattering. *Journal of Geophysical Research*, 97:101.
- Goldstein, M. L., Matthaeus, W. H., and Ambrosiano, J. J. (1986). Acceleration of charged particles in magnetic reconnection: Solar flares, the magnetosphere, and solar wind. *Geophysical Research Letters*, 13(3):205.

- Goldston, R. J. and Rutherford, P. H. (1995). *Introduction to Plasma Physics*. Institute of Physics Pub., Philadelphia, Pennsylvania.
- Innes, D. E., Inhester, B., Axford, W. I., and Wilhelm, K. (1997). Bi-directional plasma jets produced by magnetic reconnection on the sun. *Nature*, 386:811.
- Ji, H., Toyama, H., Yamagishi, K., Shinohara, S., Fujisawa, A., and Miyamoto, K. (1991). Probe measurements on the repute-1 reversed field pinch. *Review of Scientific Instrumentation*, 62:2326.
- Krall, N. A. and Trivelpiece, A. W. (1973). *Principles of Plasma Physics*. McGraw-Hill, New York.
- Leal-Quiros, E. and Prelas, M. A. (1988). An enhancement of ion energy spectra resolution and sensitivity in a multigridded energy analyser with a retarding grid potential: The variable energy analyser (vea). *IEEE Transactions on Plasma Science*, 16(6):661.
- Masuda, S., Kosugi, T., Hara, H., Tsuneta, S., and Ogawara, Y. (1994). A loop-top hard x-ray source in a compact solar flare as evidence for magnetic reconnection. *Nature*, 371:495.
- Matthaeus, W. H., Ambrosiano, J. J., and Goldstein, M. L. (1984). Particle acceleration by turbulent magnetic field reconnection. *Physical Review Letters*, 53:1449.
- Matthaeus, W. H. and Lamkin, S. L. (1986). Turbulent magnetic reconnection. *Physics of Fluids*, 29:2513.
- Miyamoto, K. (1980). *Plasma Physics for Nuclear Fusion*. MIT Press, Cambridge, Massachusetts.
- Ono, Y., Morita, A., Katsurai, M., and Yamada, M. (1993). Experimental investigation of three-dimensional magnetic reconnection by use of two colliding spheromaks. *Physics of Fluids B*, 5(10):3691.
- Ono, Y., Yamada, M., Akao, T., Tajima, T., and Matsumoto, R. (1996). Ion acceleration and direct ion heating in three-component magnetic reconnection. *Physical Review Letters*, 76:3328.
- Parker, E. N. (1957). Sweet's mechanism for merging magnetic fields in conducting fluids. *Journal of Geophysical Research*, 62:509.
- Parker, E. N. (1994). *Spontaneous Current Sheets in Magnetic Fields: With Applications to Stellar X-rays*. Oxford, New York.
- Schaffer, M. J. (1987). Exponential Taylor states in circular cylinders. *Physics of Fluids*, 30(1):160.
- Shay, M. A., Drake, J. F., Denton, R. E., and Biskamp, D. (1997). Structure of the dissipation region during collisionless magnetic reconnection. *submitted to Journal of Geophysical Research*.

- Shibata, K. (1995). Hot plasma ejection associated with compact-loop solar flares. *Astrophysical Journal*, 451:L83.
- Simpson, J. A. (1961). Design of retarding field energy analysers. *IEEE Transactions on Plasma Science*, 32(12):1283.
- Sweet, P. A. (1958). The neutral point theory of solar flares. In Lehnert, B., editor, *Electromagnetic Phenomena in Cosmical Physics*. Cambridge University Press, London.
- Taylor, J. B. (1986). Relaxation and magnetic reconnection in plasmas. *Review of Modern Physics*, 58(3):741.
- Thomas, J., Hwang, D. Q., Horton, R. D., Rogers, J. H., and Raman, R. (1993). A simple fast pulse gas valve using a dynamic pressure differential as the primary closing mechanism. *Review of Scientific Instrumentation*, 64(6):1410.
- Yamada, M., Ji, H., Hsu, S., Carter, T., Kulsrud, R., Ono, Y., and Perkins, F. (1997). Identification of y-shaped and o-shaped diffusion regions during magnetic reconnection in a laboratory plasma. *Physical Review Letters*, 78:3117.
- Yamada, M., Perkins, F. W., MacAulay, A. K., Ono, Y., and Katsurai, M. (1991). Initial results from investigation of three-dimensional magnetic reconnection in a laboratory plasma. *Physics of Fluids B*, 3(8):2379. (Invited paper from 1990 APS/DPP Meeting).